Control Design of Grid Synchronization Systems for Grid-Tied Power Converters Using Symmetrical Optimum Method: A Comprehensive Reference

Saeed Golestan, *Senior Member, IEEE*, Josep M. Guerrero, *Fellow, IEEE*, Juan C. Vasquez, *Senior Member, IEEE*, Abdullah M. Abusorrah, *Senior Member, IEEE*, Vinod Khadkikar, *Fellow, IEEE*, and Jose Rodriguez, *Life Fellow, IEEE*

***Abstract*—Control design of advanced grid synchronization systems is complex as they are often adaptive nonlinear feedback systems with one or more filtering networks and feedback loops in their structure. This article intends to contribute to addressing this issue. It is shown that the phase or frequency estimation loop of many advanced grid synchronization systems, including 3ϕ and 1ϕ phase-locked loops and frequency-locked loops equipped with in-loop filters and prefilters, can be well-approximated by a standard type-2 control system in the low-frequency range and an extension of the symmetrical optimum (SO) approach could be used to efficiently tune their control parameters. To better understand all this, an overview of the SO method and its extended version is provided and several case studies are presented. The limitations of this design approach and possible solutions are also discussed.**

***Index Terms*—Control tuning, frequency-locked loops (FLLs), linear modeling, linear time invariant (LTI) model, linear time-periodic (LTP) model, phase-locked loops (PLLs), symmetrical optimum method, synchronization systems.**

I. Grid Synchronization Systems

THERE are several ways to implement a synchronization system for a grid-tied power converter. A conventional method is using the synchronous reference frame phase-locked loop (SRF-PLL). The SRF-PLL, however, has limited performance under adverse grid scenarios as it cannot efficiently filter grid voltage disturbances. Numerous advanced PLLs have been developed as solutions to this problem in the literature [1], [2]. These PLLs are often designed by including different filters in the SRF-PLL structure. An alternative way is using other design concepts in the implementation of the grid synchronization system. For instance, the frequency-locked loop (FLL) concept has received much attention recently [3], [4], [5], [6], [7], [8], [9], [10]. A grid synchronization FLL can be understood as an adaptive complex filter centered at the fundamental grid frequency that uses an observer to estimate the grid frequency and adapt this filter to grid frequency changes. Interested readers are referred to [1], [2], [3], [4] for detailed information about basic and advanced PLLs and FLLs.

The nonlinear complex structure of advanced PLLs and FLLs, which often includes one or more adaptive filtering networks and feedback loops, makes their control tuning complicated. To address this difficulty, some methods have been proposed in the literature. A particularly interesting method is the extended symmetrical optimum (ESO) method, which ensures a maximum phase margin (PM) for the grid synchronization system (see Section II). For instance, in [11], the application of the ESO method to design the control parameters of a standard PLL with an in-loop moving-average filter (MAF) is presented. In [12], a similar work but for a chain of second-order notch filters (NFs) as the PLL's in-loop filter (IF) is presented.

The application of the ESO tuning method seems to be mostly limited to some particular PLLs, especially PLLs with an IF. This article mainly aims to show that this efficient tuning rule is broadly applicable to a wide variety of advanced PLLs and FLLs. The key idea is that one may mathematically represent many advanced grid synchronization systems as a PLL with an IF and then apply the ESO tuning rule for designing their control parameters. To clarify this idea, several case studies are presented and discussed. It needs to be emphasized here that the scope of application of this article is limited to grid-tied power converters, where the grid synchronization system often needs to have a low bandwidth (typically, lower than the fundamental frequency) to ensure a satisfactory performance in terms of stability and noise immunity.

Manuscript received 20 October 2022; revised 19 January 2023 and 15 March 2023; accepted 22 April 2023. Date of publication 4 July 2023; date of current version 22 September 2023. This work was supported in part by the Deanship of Scientific Research (DSR), King Abdulaziz University, Jeddah under Grant RG-11-135-43, in part by VILLUM FONDEN under the VILLUM Investigator under Grant 25920, in part by the Center for Research on Microgrids (CROM), and in part by the ANID under Grants FB0008, 1210208, and 1221293. Recommended for publication by Associate Editor Y. Li. *(Corresponding author: Saeed Golestan.)*

Saeed Golestan, Josep M. Guerrero, and Juan C. Vasquez are with the The Villum Center for Research on Microgrids (CROM), AAU Energy, Aalborg University, 9220 Aalborg East, Denmark (e-mail: sgd@energy.aau.dk; joz@energy.aau.dk; juq@energy.aau.dk).

Abdullah M. Abusorrah is with the Center of Research Excellence in Renewable Energy and Power Systems, Department of Electrical and Computer Engineering, Faculty of Engineering, K. A. CARE Energy Research and Innovation Center, King Abdulaziz University, Jeddah 21589, Saudi Arabia (e-mail: aabusorrah@kau.edu.sa).

Vinod Khadkikar is with the Advanced Power and Energy (APEC) and Khalifa University Space Technology and Innovation (KUSTIC) centers, Electrical Engineering and Computer Science Department, Khalifa University, Abu Dhabi 127788, UAE (e-mail: vkhadkikar@gmail.com).

Jose Rodriguez is with the Faculty of Engineering Universidad San Sebastian Santiago, Concepción 4030000, Chile (e-mail: jose.rodriguezp@uss.cl).

Color versions of one or more figures in this article are available at https://doi.org/10.1109/TPEL.2023.3292306.

Digital Object Identifier 10.1109/TPEL.2023.3292306

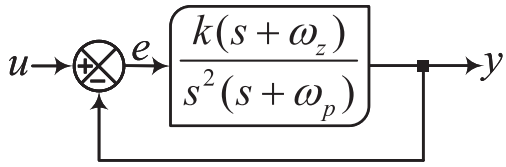

Fig. 1. A standard type-2 control system.

The rest of this article is organized as follows. In Section II, the ESO method is briefly explained and a review of its application to design the control parameters of a 3ϕ PLL with an IF is presented. In Section III, it is demonstrated that the ESO tuning method is broadly applicable to design the control parameters of 3ϕ PLLs with a prefilter (PF). In Sections IV, V, and VI, the control design of 1ϕ PLLs, type-3 grid synchronization systems, and FLLs using the ESO tuning rule is discussed, respectively. In Sections VII and VIII, some limitations of the ESO tuning rule are discussed and some possible solutions are proposed. Section IX will discuss control design considerations in a weak grid scenario, as well as in applications where a low-sampling frequency or a high control bandwidth is desired. Finally, Section X concludes this article.

II. ESO Method and Its Application for Control Tuning of 3ϕ PLLs With an IF

A. Overview of ESO Method

In 1958, Kessler [13], [14] developed the SO method for tuning control parameters of type-2 control systems, i.e., control systems with two open-loop poles at the origin. The key idea behind the SO method is to set the control parameters in a way that will ensure the magnitude-frequency response of the closed-loop transfer function (TF), $G_{cl}(s)$, is as close to one as possible at low frequencies. Mathematically, this idea corresponds to make $G_{cl}(0) = 1$ and $\frac{d^n|G_{cl}(j\omega)|}{d\omega^n} = 0$ at $\omega = 0$ for as many n as possible [15].

To better understand the properties of the SO tuning rule, consider Fig. 1, which shows a simple type-2 control system. The open- and closed-loop TFs of this control system are

$$G_{ol}(s) = \frac{y(s)}{e(s)} = \frac{k(s+\omega_z)}{s^2(s+\omega_p)} \tag{1}$$

$$G_{cl}(s) = \frac{y(s)}{u(s)} = \frac{k(s+\omega_z)}{s^3 + \omega_p s^2 + ks + k\omega_z} \tag{2}$$

where, ω_z and ω_p are the corner frequencies and k is a constant. After some calculations, we get

$$|G_{cl}(j\omega)| = \frac{k\sqrt{\omega^2+\omega_z^2}}{\sqrt{\omega^6 + (\omega_p^2 - 2k)\omega^4 + (k^2 - 2k\omega_p\omega_z)\omega^2 + k^2\omega_z^2}}. \tag{3}$$

Because of the zero in the numerator, the magnitude of the closed-loop TF cannot be made maximally flat at $\omega = 0$. However, if the parameters are selected such that the coefficients of ω^2 and ω^4 in the denominator (3) become zero [see (4)], $|G_{cl}(j\omega)|$ becomes as close to one as possible at low frequencies

$$\begin{aligned} k &= 2\omega_c^2 \\ \omega_p &= 2\omega_c \\ \omega_z &= \omega_c/2 \end{aligned} \tag{4}$$

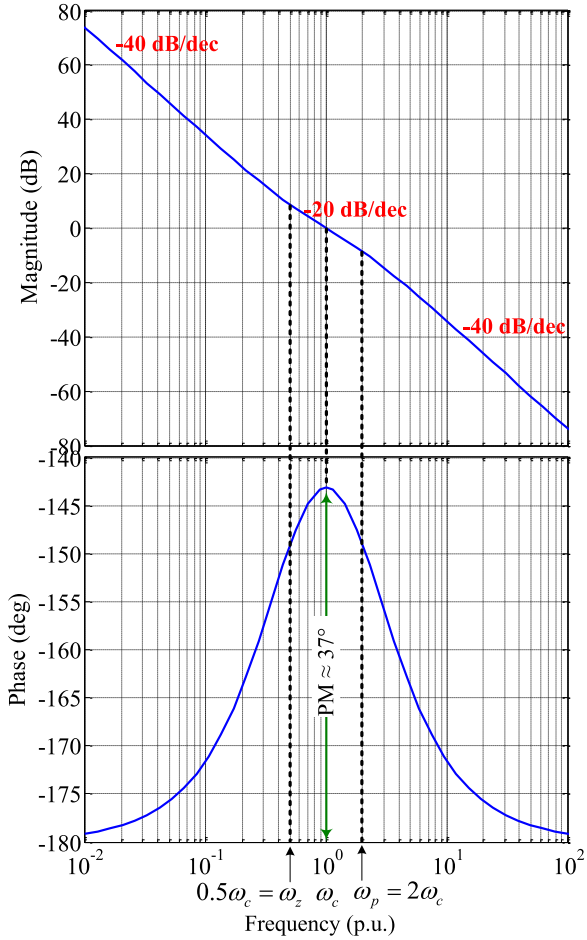

Fig. 2. Bode diagram of the open-loop TF (1). The control parameters are selected according to (4). The frequency axis is normalized with respect to the gain crossover frequency ω_c.

The abovementioned tuning rule results in some properties that are summarized as follows.

1) The open-loop frequency response is symmetrical around the gain crossover frequency ω_c. Fig. 2, which shows the Bode plot of the open-loop TF (1), clearly shows this symmetry. Note that the name *symmetrical optimum* is motivated by this symmetry.
2) The gain crossover frequency occurs at the geometric mean of the corner frequencies, i.e., $\omega_c = \sqrt{\omega_z\omega_p}$.
3) The PM is independent of ω_c and fixed at about 37°.

The achieved PM is relatively low, causing a large step response overshoot, around 43%. To deal with this problem, a modification of the SO tuning rule, called the ESO method, is suggested in [16]. The ESO method, similar to the SO method, maintains the symmetry of open-loop frequency response around ω_c by setting $\omega_c = \sqrt{\omega_z\omega_p}$. The difference is

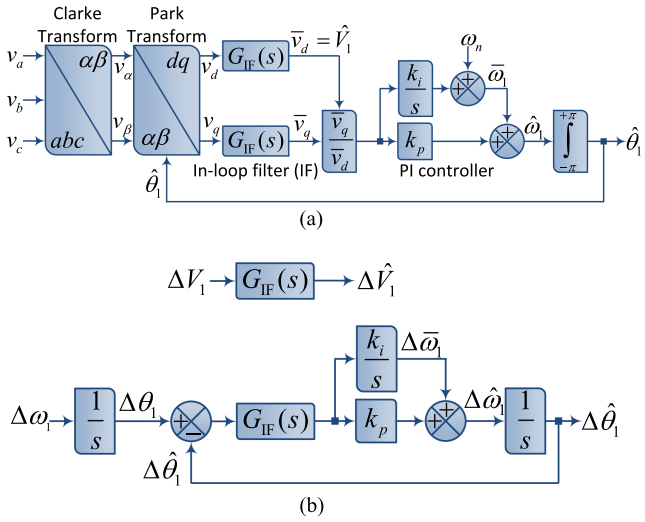

Fig. 3. (a) Standard 3ϕ PLL with an IF. (b) Its LTI model.

that the corner frequencies ω_z and ω_p may be moved to lower and higher frequency regions, respectively, to increase the PM. If we assume that $\omega_p = b^2\omega_z$, where b is a design constant, the ESO tuning rule is expressed as

$$\begin{aligned} k &= b\omega_c^2 \\ \omega_p &= b\omega_c \\ \omega_z &= \omega_c/b. \end{aligned} \tag{5}$$

Note that the SO tuning rule in (4) is a special case of the ESO rule with $b = 2$. A striking feature of the ESO tuning rule is that it makes the PM a function of the design constant b, as shown in the following:

$$\text{PM} = \tan^{-1}\left(\frac{b^2-1}{2b}\right). \tag{6}$$

Therefore, by designing the constant b appropriately, one may increase the PM and reduce the step-response overshoot. For instance, selecting $b = 1+\sqrt{2}$ and $b = 2+\sqrt{3}$, which are corresponding to $\text{PM} = 45^\circ$ and $\text{PM} = 60^\circ$, respectively, reduces the step-response overshoot to around 34% and 19%, respectively.

Sometimes, due to some constraints and/or design considerations, the corner frequency ω_p is already fixed. In such cases, the ESO tuning rule in (5) can be rewritten as

$$\begin{aligned} k &= \omega_p^2/b \\ \omega_z &= \omega_p/b^2. \end{aligned} \tag{7}$$

B. Control Tuning of a Standard 3ϕ PLL With an IF

A large number of advanced 3ϕ PLLs include a standard SRF-PLL and an IF [1], [17], [18]. Fig. 3(a) shows a general structure of such PLLs. In this structure, the 3ϕ input signal v_{abc} is first transferred to the *dq* frame and passed through an IF to block/attenuate disturbance components. Then, an amplitude normalization is used to mitigate the impact of variations in the grid voltage amplitude on the PLL stability/dynamic behavior. Other elements in the PLL include a proportional-integral (PI) controller and an integrator, which represent the PLL loop filter and voltage-controlled oscillator, respectively.

Based on the guidelines provided in [1], one can linearize the PLL in Fig. 3(a) and obtain a linear time-invariant (LTI) model, as shown in Fig. 3(b), where the prefix Δ denotes a small perturbation. The resulting model is a two-inputs-two-outputs (TITO) system. Therefore, it has two PMs and two gain margins (GMs), which are determined by the open-loop transfer matrix as follows:

$$\begin{bmatrix} \Delta\hat{V}_1(s) \\ \Delta\hat{\theta}_1(s) \end{bmatrix} = \begin{bmatrix} \overbrace{\dfrac{G_{\text{IF}}(s)}{1-G_{\text{IF}}(s)}}^{G_{ol}^{V_1}(s)} & 0 \\ 0 & \underbrace{G_{\text{IF}}(s)\dfrac{k_p s + k_i}{s^2}}_{G_{ol}^{\theta_1}(s)} \end{bmatrix} \times \begin{bmatrix} \Delta V_1(s) - \Delta\hat{V}_1(s) \\ \Delta\theta_1(s) - \Delta\hat{\theta}_1(s) \end{bmatrix}. \tag{8}$$

Fortunately, the PM and GM of the amplitude estimation loop are almost always greater than those of the phase estimation loop (PEL). Therefore, in designing control parameters, one just needs to ensure that the PEL has a good stability margin.

A key element in the open-loop TF $G_{ol}^{\theta_1}(s)$ is $G_{\text{IF}}(s)$, which can be an *n*-order infinite-impulse-response (IIR) low-pass filter (LPF) [19], a chain of second-order IIR NFs [12], [20], a chain of *dq*-frame delayed signal cancellation (*dq*DSC) operators [18], [21], and a moving average filter (MAF) [11], [22], just to mention a few. The TFs of these filters are given in Table I. The interesting point is that all these filters are approximated well in low frequencies by a first-order TF as $G_{\text{IF}}(s) \approx \frac{1}{\tau s+1}$ (see Table I). Note that to find this approximation, one or more of the following steps may need to be performed.

1) Neglect the second- and higher order frequency terms.
2) Replace delay terms with their first-order Padé approximation.
3) Approximate the product of first-order lag filters with time constants τ_i $(i = 1, 2, \ldots, m)$ with a first-order lag filter with the time constant $\sum_{i=1}^{m}\tau_i$.

Once the first-order approximation of the IF is obtained, $G_{ol}^{\theta_1}(s)$ can be rewritten as

$$G_{ol}^{\theta_1}(s) \approx \frac{1}{\tau s+1}\frac{k_p s + k_i}{s^2} = \frac{\overbrace{(k_p/\tau)}^{k}(s+\overbrace{k_i/k_p}^{\omega_z})}{s^2\underbrace{(s+1/\tau)}_{\omega_p}}. \tag{9}$$

The abovementioned TF is the same as (1). Therefore, the ESO tuning rule is applicable to design the control parameters. Note that the control parameter(s) of an IF often need(s) to be selected before tuning the PI gains k_p and k_i. The main criteria for this selection are the concerned disturbance components and the range of grid frequency variations (in the case that the IF is not frequency adaptive). A predesigned IF means that the time constant τ (and therefore ω_p) in (9) is already fixed and

TABLE I
DESIGNING THE CONTROL PARAMETERS OF A STANDARD 3ϕ PLL EQUIPPED WITH AN IF BASED ON THE ESO TUNING RULE

Control Tuning of PLLs equipped with an IF			
IF			**Tuning result**
Type	**TF**	**First-order approximation**	
***n*-order IIR LPF**	$G_{\rm IF}(s)=\frac{a_n\omega_l^n}{a_0s^n+a_1\omega_l s^{n-1}+\cdots+a_{n-1}\omega_l^{n-1}s+a_n\omega_l^n}$	$G_{\rm IF}(s)\approx\frac{a_n\omega_l^n}{a_{n-1}\omega_l^{n-1}s+a_n\omega_l^n}=\underbrace{\frac{1}{(a_{n-1}/\omega_l a_n)}}_{\tau}s+1$	$k_p=\frac{1}{b\tau}$ $k_i=\frac{1}{b^3\tau^2}$
Cascaded IIR NFs	$G_{\rm IF}(s)=\prod_{i=1}^{m}\frac{s^2+\omega_{h_i}^2}{s^2+(\omega_{h_i}/Q_{h_i})s+\omega_{h_i}^2}$	$G_{\rm IF}(s)\approx\prod_{i=1}^{m}\frac{1}{\frac{1}{Q_{h_i}\omega_{h_i}}s+1}\approx\underbrace{\frac{1}{\left(\sum_{i=1}^{m}\frac{1}{Q_{h_i}\omega_{h_i}}\right)}}_{\tau}s+1$	
Cascaded *dq*DSC operators	$G_{\rm IF}(s)=\prod_{i=1}^{m}\frac{1+e^{-\frac{T}{n_i}s}}{2}$	$G_{\rm IF}(s)\approx\prod_{i=1}^{m}\frac{1}{\left(\frac{T}{2n_i}\right)s+1}\approx\underbrace{\frac{1}{\left(\frac{T}{2}\sum_{i=1}^{m}\frac{1}{n_i}\right)}}_{\tau}s+1$	
MAF	$G_{\rm IF}(s)=\frac{1-e^{-T_w s}}{T_w s}$	$G_{\rm IF}(s)\approx\underbrace{\frac{1}{(T_w/2)}}_{\tau}s+1$	

***n*-order IIR LPF**: ω_l, n, and a_i $(i=0,1,\cdots,n)$ denote the LPF cutoff frequency, order, and coefficients, respectively.
Cascaded IIR NFs: ω_{h_i} and Q_{h_i} $(i=1,\cdots,m)$ denote the notch frequency and quality factor of the NF, respectively, and m is the number of the NFs.
Cascaded *dq*DSC operators: n_i $(i=1,\cdots,m)$ are the delay factors, T is the grid voltage fundamental period, and m is the number of the *dq*DSC operators.
MAF: T_w is the MAF window length.

the ESO tuning rule in (7) may be deployed. Applying this tuning rule determines the PLL's proportional and integral gains k_p and k_i as

$$\begin{matrix} k=\frac{k_p}{\tau}=\frac{1}{b\tau^2} \\ \omega_z=\frac{k_i}{k_p}=\frac{1}{b^2\tau}\end{matrix}\Rightarrow\begin{matrix} k_p=\frac{1}{b\tau} \\ k_i=\frac{1}{b^3\tau^2}.\end{matrix}\tag{10}$$

Provided that the time-constant τ is already fixed, the design constant b is the only degree of freedom in designing k_p and k_i. Recall that b determines the PM [see (6)]. Therefore, one may determine k_p and k_i by choosing an appropriate PM for the PLL's PEL. $\rm PM=45^\circ$, which corresponds to $b=1+\sqrt{2}$, is suitable here because it results in an optimum damping factor $1/\sqrt{2}$ for the closed-loop complex-conjugate poles of the PEL of the PLL. If a more damped dynamic response is needed, a larger value for the design constant b (for instance, $b=2+\sqrt{3}$, corresponding to $\rm PM=60^\circ$) may be chosen.

In summary, the following step-by-step procedure for tuning the control parameters of a 3ϕ PLL equipped with an IF is suggested.

1) Design the control parameter(s) of the specified IF based on the required level of noise immunity.
2) Approximate the IF's TF in the low-frequency range by a first-order TF as $G_{\rm IF}(s)\approx\frac{1}{\tau s+1}$ (see Table I for some examples).
3) Apply the ESO tuning rule and select the proportional and integral gains as $k_p=\frac{1}{b\tau}$ and $k_i=\frac{1}{b^3\tau^2}$ [see (10) and Table I].
4) Select the design constant b based on the required PM [see (6)].
5) Calculate the proportional and integral gains according to the definitions in step 3.
6) Test the PLL numerically to ensure its performance is satisfactory. If the performance is not satisfactory return to step 1 and redesign the IF. For instance if the dynamic response is slow, try to increase the IF's bandwidth or consider other types of IF (if possible), and if the noise immunity is not satisfactory, try to reduce the IF's bandwidth or increase its attenuation around the concerned frequencies.

To gain a better understanding of the abovementioned procedure, several design examples are presented in Table II. Note that $b=1+\sqrt{2}$, which corresponds to $\rm PM=45^\circ$, is considered.

Fig. 4(a)–(c) show that the Bode plots of the IFs designed in Table II and their first-order approximations. It is observed that they have a close frequency response in the low-frequency range. In Fig. 5(a)–(c), the open-loop Bode plots of the PEL of the designed PLLs in Table II are observed. These plots indicate that the PM of the designed PLLs is very close to the targeted one, i.e., $\rm PM=45^\circ$. Note that the small difference between the achieved and targeted PMs is due to using the first-order approximation of the IF in the design procedure.

In Fig. 6(a), a comparison between the designed PLLs under a phase jump test is shown. Note that all PLLs have almost the same phase overshoot (around 36%) as they have almost the same PM. However, they have different speeds of response. The reason is that they have different IFs with different low-frequency phase delays and, therefore, different bandwidths. For instance, the PLL designed for Scenario 3 has the slowest dynamic response as its IF (i.e., MAF with $T_w=0.02$ s) causes more phase delay compared to other IFs.

In Fig. 6(b), a comparison between the designed PLLs under an adverse grid condition (Scenario 1 in Table II) is shown. In this test, the grid frequency is fixed at 45 Hz, and the magnitude of all harmonics is 5%. It is observed that the PLLs designed for Scenario 1 and 3 have the worst and best performance, respectively, as they have the highest and lowest bandwidths.

An important question arises here: Is the ESO tuning rule applicable to other grid synchronization systems, e.g., other families of PLLs or FLL-based grid synchronization systems? The short answer is: Yes, but a problem transformation may be required. The problem transformation method suggests that a

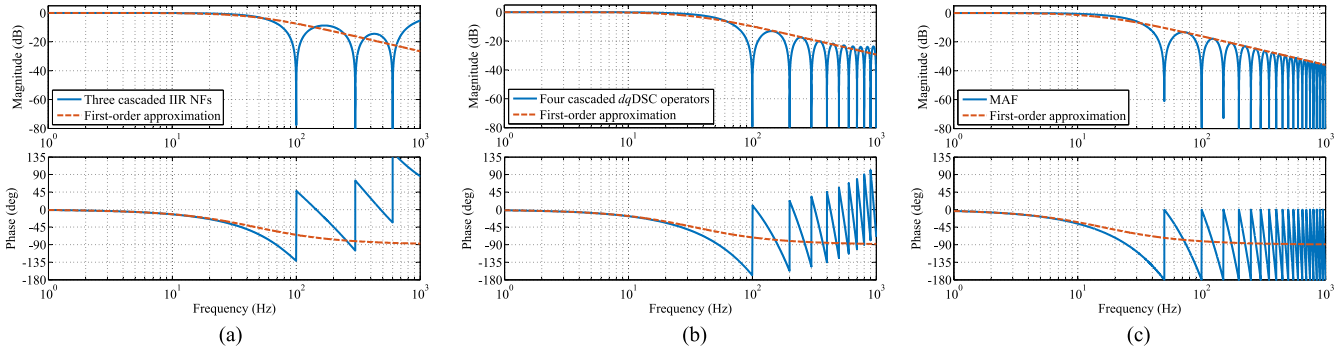

Fig. 4. Comparison of the frequency response of the IFs selected for (a) Scenario 1, (b) Scenario 2, and (c) Scenario 3 in Table II with their first-order counterparts.

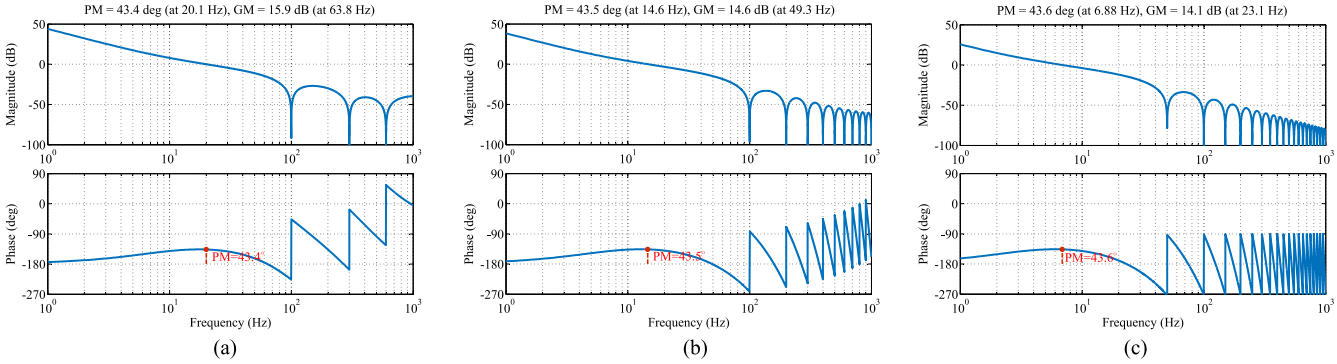

Fig. 5. Open-loop Bode plots of the PEL of the PLLs designed for (a) Scenario 1, (b) Scenario 2, and (c) Scenario 3 in Table II.

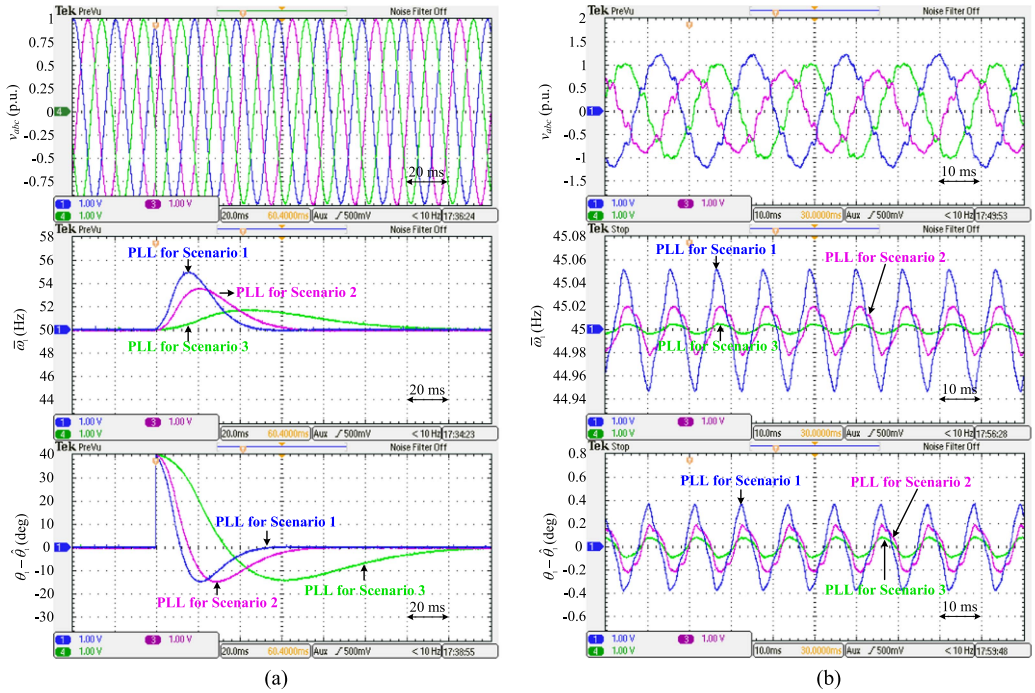

Fig. 6. Comparison of the PLLs designed for scenarios 1, 2, and 3 under (a) 40° phase jump test and (b) an imbalanced and harmonically distorted grid condition. These results are obtained using a dSPACE platform. v_{abc} is generated internally in the dSPACE.

TABLE II
DESIGN EXAMPLES

Design examples			
Concerned disturbances	**Selected IF (its parameters)**	**First-order approximation of IF**	**PI controller gains**
Scenario 1 Grid voltage imbalance plus harmonics of order -5,+7,-11,+13	Three cascaded IIR NFs ($Q_{h_1}=Q_{h_2}=Q_{h_3}=\frac{1}{\sqrt{2}}$, $w_{h_1}=2\pi 100$ $w_{h_2}=2\pi 300$, $w_{h_3}=2\pi 600$ rad/s)	$G_{\rm IF}(s)\approx \frac{1}{\left(\sum_{i=1}^{3}\frac{1}{Q_{h_i}\omega_{h_i}}\right)s+1}=\underbrace{\frac{1}{(3.38e-3)}}_{\tau}\,s+1$	$k_p=\frac{1}{b\tau}=122.7$ $k_i=\frac{1}{b^3\tau^2}=6232.9$
Scenario 2 Grid voltage imbalance plus all odd-order harmonics	Four cascaded dqDSC operators ($T=0.02$ s, $n_i=2^{i+1}$, $i=1,\cdots,4$)	$G_{\rm IF}(s)\approx \frac{1}{\left(\frac{T}{2}\sum_{i=1}^{4}\frac{1}{n_i}\right)s+1}=\underbrace{\frac{1}{(4.69e-3)}}_{\tau}\,s+1$	$k_p=\frac{1}{b\tau}=88.4$ $k_i=\frac{1}{b^3\tau^2}=3234.4$
Scenario 3 Grid voltage imbalance plus all harmonics	MAF ($T_w=0.02$ s)	$G_{\rm IF}(s)\approx \frac{1}{(T_w/2)s+1}=\underbrace{\frac{1}{0.01}}_{\tau}\,s+1$	$k_p=\frac{1}{b\tau}=41.4$ $k_i=\frac{1}{b^3\tau^2}=710.7$

problem that may not be solved easily and/or directly can be transformed into a problem that we know how to solve. The same idea is adopted in this article. We try to transform different grid synchronization systems to the form of a PLL with an IF, and then apply the ESO tuning rule.

III. 3ϕ PLLs EQUIPPED WITH A PF

Many advanced PLLs are basically consisted of a standard SRF-PLL and a PF [23], [24], [25]. Fig. 7(a) shows a typical structure of such PLLs. In this structure, the PF has the responsibility of filtering disturbance components before the SRF-PLL input and extracting the fundamental positive-sequence component of the grid voltage. The phase, frequency, and amplitude of this component are then estimated by the SRF-PLL. To adapt the PF to variations in the grid frequency, it is often necessary to feed back the SRF-PLL output frequency to the PF.

A. Tuning

The input–output relation of the PF in Fig. 7(a) may be described in the time domain as

$$\underbrace{\hat{v}_{\alpha,1}+j\hat{v}_{\beta,1}}_{\hat{\boldsymbol{v}}_{\boldsymbol{\alpha\beta},\mathbf{1}}}=\boldsymbol{G}_{\mathbf{PF}}(\rho)\underbrace{[v_\alpha+jv_\beta]}_{\boldsymbol{v}_{\boldsymbol{\alpha\beta}}} \tag{11}$$

where, $\rho=d/dt$ and $\boldsymbol{G}_{\mathbf{PF}}(\rho)$ is a complex time-domain operator. Note that ρ corresponds to the Laplace operator s in the frequency domain if the PF is LTI.

Based on Fig. 7(a), we get

$$\begin{aligned}\underbrace{\bar{v}_d+j\bar{v}_q}_{\bar{\boldsymbol{v}}_{\boldsymbol{dq}}}&=e^{-j\hat{\theta}_1}\hat{\boldsymbol{v}}_{\boldsymbol{\alpha\beta},\mathbf{1}}=e^{-j\hat{\theta}_1}\boldsymbol{G}_{\mathbf{PF}}(\rho)\boldsymbol{v}_{\boldsymbol{\alpha\beta}}\\&=e^{-j\hat{\theta}_1}\boldsymbol{G}_{\mathbf{PF}}(\rho)e^{j\hat{\theta}_1}\underbrace{(v_d+jv_q)}_{\boldsymbol{v}_{\boldsymbol{dq}}=e^{-j\hat{\theta}_1}\boldsymbol{v}_{\boldsymbol{\alpha\beta}}}\\&=\underbrace{\boldsymbol{G}_{\mathbf{PF}}(\rho+j\hat{\omega}_1)}_{\boldsymbol{G}_{\mathbf{IF}}(\rho)}\boldsymbol{v}_{\boldsymbol{dq}}.\end{aligned} \tag{12}$$

The abovementioned relation demonstrates that the PLL in Fig. 7(a) is mathematically equivalent to a PLL with the IF $\boldsymbol{G}_{\mathbf{IF}}(\rho)=\boldsymbol{G}_{\mathbf{PF}}(\rho+j\hat{\omega}_1)$, as shown in Fig. 7(b) [26].

By breaking $\boldsymbol{G}_{\mathbf{IF}}(\rho)$ into its real and imaginary parts, i.e., $\boldsymbol{G}_{\mathbf{IF}}(\rho)=G_r(\rho)+jG_i(\rho)$, Fig. 7(b) can be represented as

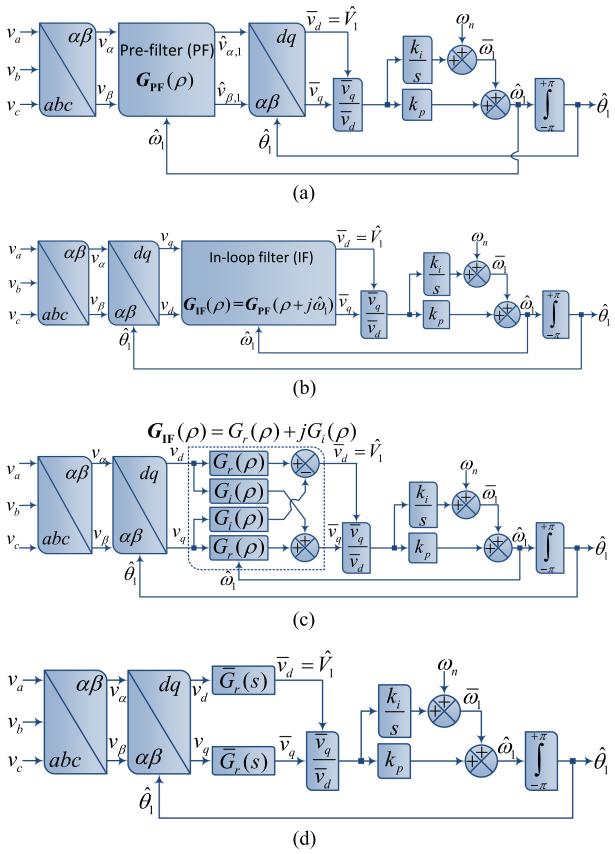

Fig. 7. (a) Standard 3ϕ PLL with a PF, and (b) its IF-form equivalent. (c) Alternative representation, which is obtained by breaking $\boldsymbol{G}_{\mathbf{IF}}(\rho)$ into its real and imaginary parts. (d) Simplified IF-form version. $\rho=d/dt$. This operator corresponds to the Laplace operator s in the frequency domain if we are dealing with LTI systems.

Fig. 7(c). Note that the imaginary part $G_i(\rho)$ causes a cross-coupling between the d- and q-axis. This coupling often has a negligible effect at low frequencies. By neglecting this coupling and linearizing the nonlinearity caused by the frequency feedback loop, Fig. 7(c) can be simplified, as shown in Fig. 7(d), in which $\bar{G}_r$ denotes the linearized version of G_r. This structure is the same as Fig. 3(a). Therefore, we can deploy the same procedure described in Section II-B to tune the control parameters.

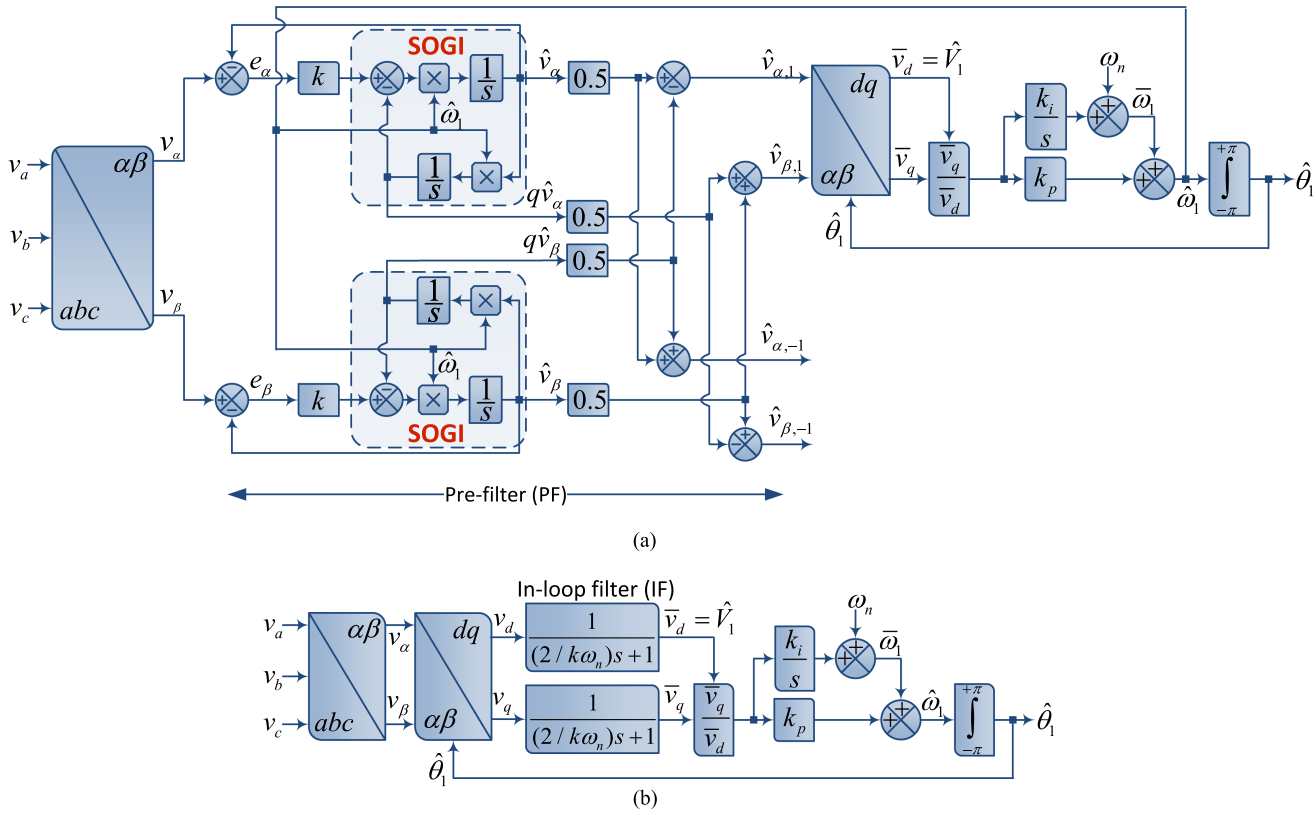

Fig. 8. (a) DSOGI-PLL. (b) Simplified IF-form counterpart of the DSOGI-PLL. k is the SOGI gain.

The proposed method for tuning the control parameters of a 3ϕ PLL with a PF can be summarized as follows.

1) Describe the input–output relationship of the PLL's PF as $\hat{\boldsymbol{v}}_{\boldsymbol{\alpha\beta},\mathbf{1}} = \boldsymbol{G}_{\mathbf{PF}}(\rho)\boldsymbol{v}_{\boldsymbol{\alpha\beta}}$ [see (11)].
2) Obtain the IF-form equivalent of the PLL, $\boldsymbol{G}_{\mathbf{IF}}(\rho) = \boldsymbol{G}_{\mathbf{PF}}(\rho + j\hat{\omega}_1)$ [see Fig. 7(b)].
3) Break $\boldsymbol{G}_{\mathbf{IF}}(\rho)$ into its real and imaginary parts, i.e., $\boldsymbol{G}_{\mathbf{IF}}(\rho) = G_r(\rho) + jG_i(\rho)$, neglect the imaginary part $G_i(\rho)$, and linearize possible nonlinearities caused by the frequency feedback loop in the real part $G_r(\rho)$.
4) Follow the ESO-based method presented in Section II-B for tuning the control parameters.

To better understand the abovementioned procedure, a design example is presented in the following.

B. Design Example

Consider the PLL in Fig. 8(a), which is known as the dual second-order generalized integrator-based PLL (DSOGI-PLL) [27]. Two SOGI-based quadrature signal generators (QSGs) and a positive-negative-sequence calculator constitute the PF of the DSOGI-PLL. Note that we have to first transform the DSOGI-PLL to a structure similar to Fig. 7(d), and then apply the ESO tuning rule presented in Section II-B.

The time-domain input–output relationship of the PF in Fig. 8(a) is

$$\hat{\boldsymbol{v}}_{\boldsymbol{\alpha\beta},\mathbf{1}} = \underbrace{\frac{0.5k\hat{\omega}_1(\rho + j\hat{\omega}_1)}{\rho^2 + k\hat{\omega}_1\rho + \hat{\omega}_1^2}}_{\boldsymbol{G}_{\mathbf{PF}}(\rho)} \boldsymbol{v}_{\boldsymbol{\alpha\beta}}. \tag{13}$$

Note that to obtain the abovementioned relationship, $\dot{\hat{\omega}}_1 \approx 0$ has been assumed. This assumption is valid for control tuning purposes where low-frequency dynamics are concerned.

The IF-form equivalent of the abovementioned PF is

$$\boldsymbol{G}_{\mathbf{IF}}(\rho) = \boldsymbol{G}_{\mathbf{PF}}(\rho + j\hat{\omega}_1) = \frac{0.5k\hat{\omega}_1(\rho + j2\hat{\omega}_1)}{(\rho + j\hat{\omega}_1)^2 + k\hat{\omega}_1(\rho + j\hat{\omega}_1) + \hat{\omega}_1^2}. \tag{14}$$

By breaking $\boldsymbol{G}_{\mathbf{IF}}(\rho)$ into its real and imaginary parts, we get

$$\begin{aligned}\boldsymbol{G}_{\mathbf{IF}}(\rho) &= G_r(\rho) + jG_i(\rho) \\ &= \underbrace{\frac{0.5k\hat{\omega}_1(\rho^3 + k\hat{\omega}_1\rho^2 + 4\hat{\omega}_1^2\rho + 2k\hat{\omega}_1^3)}{\rho^4 + 2k\hat{\omega}_1\rho^3 + (k^2+4)\hat{\omega}_1^2\rho^2 + 4k\hat{\omega}_1^3\rho + k^2\hat{\omega}_1^4}}_{D(\rho)} \\ &\quad + j\frac{0.5k^2\hat{\omega}_1^3\rho}{D(\rho)}.\end{aligned} \tag{15}$$

Because of the time-varying nature of $\hat{\omega}_1$, which is the output frequency of the DSOGI-PLL [see Fig. 8(a)], $\boldsymbol{G}_{\mathbf{IF}}(\rho)$ in (15)

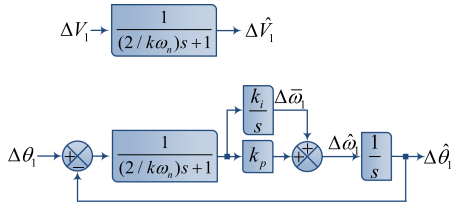

Fig. 9. Reduced-order LTI model of the DSOGI-PLL.

is nonlinear. It can be shown that this nonlinearity can be linearized by replacing $\hat{\omega}_1$ by its nominal value, i.e., ω_n. With this linearization and with neglecting the imaginary part $G_i(\rho)$, we get

$$\boldsymbol{G_{IF}}(s) \approx \overbrace{\frac{0.5k\omega_n(s^3+k\omega_n s^2+4\omega_n^2 s+2k\omega_n^3)}{s^4+2k\omega_n s^3+(k^2+4)\omega_n^2 s^2+4k\omega_n^3 s+k^2\omega_n^4}}^{\bar{G}_r(s)} \tag{16}$$

where, $\bar{G}_r$ denotes the linearized version of G_r.

It is shown in the Appendix A that (16) can be approximated in the low-frequency range with

$$\boldsymbol{G_{IF}}(s) \approx \bar{G}_r(s) \approx \underbrace{\frac{1}{(2/(k\omega_n))\,s+1}}_{\tau}. \tag{17}$$

By substituting $\bar{G}_r(s)$ in Fig. 7(d) with (17), a simplified IF-form representation of the DSOGI-PLL is obtained, as shown in Fig. 8(b). If we neglect the presence of any disturbance component in the grid voltage, Fig. 8(b) can be linearized as shown in Fig. 9. If we apply the ESO tuning rule described in Section II-B to this model [see (10)], we get

$$k_p = \frac{1}{b\tau} = \frac{k\omega_n}{2b}$$
$$k_i = \frac{1}{b^3\tau^2} = \frac{k^2\omega_n^2}{4b^3}. \tag{18}$$

The design constant b is set to $1+\sqrt{2}$, which corresponds to $\mathrm{PM}=45^\circ$. The SOGI gain k, as recommended in the literature [28], is set to $k=\sqrt{2}$. This value provides an optimal damping factor $1/\sqrt{2}$ for the PF in the extraction of the fundamental component. With these selections, we get $k_p=92$ and $k_i=3507.1$.

Using the LTI model in Fig. 9, we get

$$\begin{bmatrix}\Delta\hat{V}_1(s)\\ \Delta\hat{\theta}_1(s)\end{bmatrix} = \begin{bmatrix}\frac{1}{\frac{2}{k\omega_n}s} & 0\\ 0 & \frac{1}{\frac{2}{k\omega_n}s+1}\frac{k_p s+k_i}{s^2}\end{bmatrix}\begin{bmatrix}\Delta V_1(s)-\Delta\hat{V}_1(s)\\ \Delta\theta_1(s)-\Delta\hat{\theta}_1(s)\end{bmatrix} \tag{19}$$

which is the open-loop transfer matrix of the DSOGI-PLL. The eigenloci of this transfer matrix are shown in Fig. 10. The PM of the PEL, as expected, is 45°. The PM of the amplitude estimation loop is 90°. Both control loops have an infinite GM. The model in Fig. 9 and its open-loop transfer matrix in (19) also predict that increasing the SOGI gain k and, therefore, the proportional and integral gains k_p and k_i [see (18)] does not change these

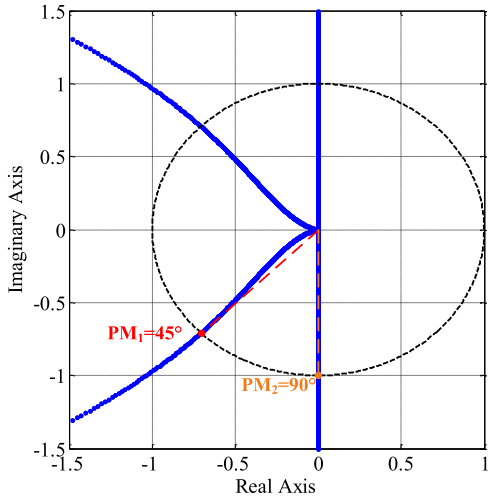

Fig. 10. Eigenloci of the open-loop transfer matrix (19). Parameters: $k=\sqrt{2}$, $b=1+\sqrt{2}$, $\omega_n=2\pi 50$ rad/s, $k_p=\frac{k\omega_n}{2b}=92$, and $k_i=\frac{k^2\omega_n^2}{4b^3}=3507.1$.

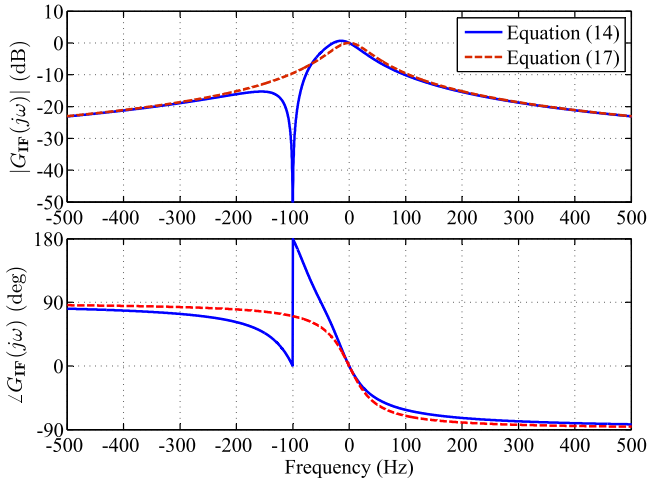

Fig. 11. Magnitude and phase characteristics of (14) and (17). $k=\sqrt{2}$.

stability margins as long as $b=1+\sqrt{2}$. The accuracy of these predictions will be examined in detail later.

To evaluate the efficiency of the tuning method, we need to examine the accuracy of (17) in approximating (14) in the low-frequency range. To this end, $\hat{\omega}_1=\omega_n$ is considered, which removes the nonlinearity of (14) and makes ρ corresponding to the Laplace operator s in the frequency domain. Fig. 11 shows the magnitude and phase characteristics of (14) and (17). To obtain these plots, $k=\sqrt{2}$ is considered. These plots verify that (17) approximates well (14) in the low-frequency range. The accuracy of the approximation is increased (reduced) for smaller (larger) values of the SOGI gain k.

The abovementioned observation can be further supported using some numerical tests. For instance, Fig. 12 provides a comparison between the DSOGI-PLL and its simplified IF-form counterpart in response to a 40° phase jump test. It is observed that they have almost the same transient responses and, therefore,

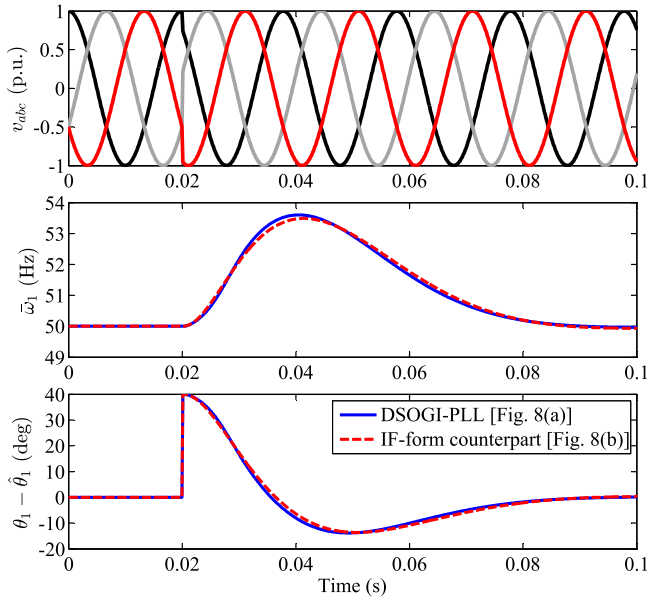

Fig. 12. Comparison between the DSOGI-PLL and its simplified IF-form counterpart in response to a 40° phase jump test.

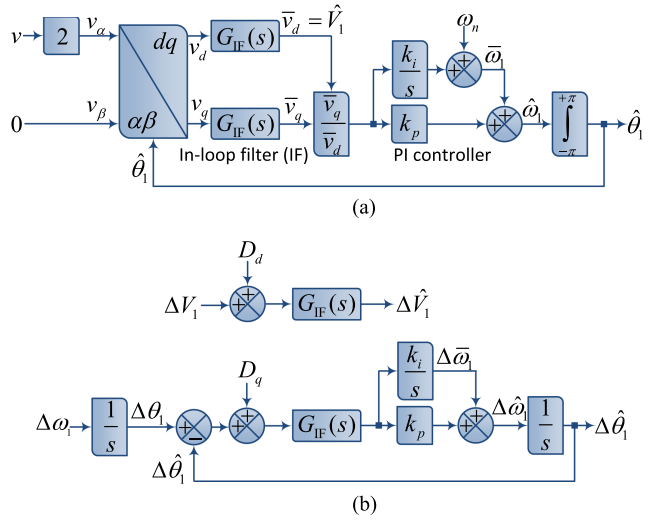

Fig. 13. (a) pPLL with an IF. (b) Its LTI model.

almost the same low-frequency dynamics. This observation also suggests that the PEL of the DSOGI-PLL has achieved almost the same PM as the targeted one, i.e., PM = 45°. This conclusion is based on this observation that the DSOGI-PLL has almost the same step-response overshoot as its IF-form counterpart. Recall that the PM and the step-response overshoot of a control system are related.

IV. 1ϕ PLLs

A. Power-Based PLL (pPPL) With an IF

Many advanced 1ϕ PLLs are basically a pPLL with an IF, as shown in Fig. 13(a) [2], [29], [30], [31]. A pPLL can be understood as an SRF-PLL with $v_\alpha = 2v$ and $v_\beta = 0$, where v is the 1ϕ input signal. To better understand how the PLL in Fig. 13(a) works, a simple study is presented as follows.

If we consider the input signal v as

$$v = V_1 \cos(\theta_1) \tag{20}$$

where, V_1 and θ_1 denote its fundamental-frequency amplitude and phase angle, respectively, the signals v_d and v_q in Fig. 13(a) can be expressed as

$$\begin{aligned} v_d &= V_1 \overbrace{\cos(\theta_1 - \hat{\theta}_1)}^{\approx 1} + V_1 \cos(\theta_1 + \hat{\theta}_1) \\ v_q &= V_1 \underbrace{\sin(\theta_1 - \hat{\theta}_1)}_{\approx(\theta_1 - \hat{\theta}_1)} - V_1 \sin(\theta_1 + \hat{\theta}_1). \end{aligned} \tag{21}$$

It is observed that the signals v_d and v_q contain a dc (or quasi dc term) and a double-frequency (disturbance) term. The IF in Fig. 13(a) is mainly responsible to block (or at least attenuate) these double-frequency terms. For instance, if an MAF is used as the IF, its window length should be set to $T_w = T/2$ or $T_w = T$ to ensure the double-frequency terms are blocked, and if a chain of IIR NFs is used as the IF, an NF with the notch frequency at twice the grid fundamental frequency should be used in the chain. The IF will also help to filter possible harmonics of the grid voltage.

Using (21), an LTI model, as shown in Fig. 13(b), can be derived for the PLL in Fig. 13(a). In this model, D_d and D_q model the double-frequency (disturbance) terms in (21). As the IF in Fig. 13(a) often blocks (or at least attenuates) the double-frequency components of the signals v_d and v_q, their effects can be neglected during the tuning procedure. With neglecting D_d and D_q, Fig. 13(b) becomes the same as Fig. 3(b), that is the LTI model of a standard 3ϕ PLL with an IF. Therefore, the same tuning process presented in Section II-B can be adopted for tuning the control parameters of a pPLL with IF.

As a design example, assume that the IF in Fig. 13(a) is a third-order butter-worth LPF

$$G_{\text{IF}}(s) = \frac{\omega_l^3}{s^3 + 2\omega_l s^2 + 2\omega_l^2 s + \omega_l^3} \tag{22}$$

where, ω_l is the cutoff frequency. According to Table I, the abovementioned TF can be approximated in the low-frequency range by

$$G_{\text{IF}}(s) \approx \frac{1}{(2/\omega_l)s + 1}. \tag{23}$$

Considering the abovementioned approximation and the LTI model in Fig. 13(b), the open-loop TF of the PEL can be obtained as

$$G_{ol}^{\theta_1}(s) = \frac{\Delta\hat{\theta}_1(s)}{\Delta\theta_1(s) - \Delta\hat{\theta}_1(s)} \approx \frac{1}{\underbrace{(2/\omega_l)}_{\tau}\, s + 1} \frac{k_p s + k_i}{s^2}. \tag{24}$$

The abovementioned TF is the same as (9). Therefore, according to (10), the proportional and integral gains k_p and k_i can be designed as

$$k_p = \frac{1}{b\tau} = \frac{\omega_l}{2b}$$

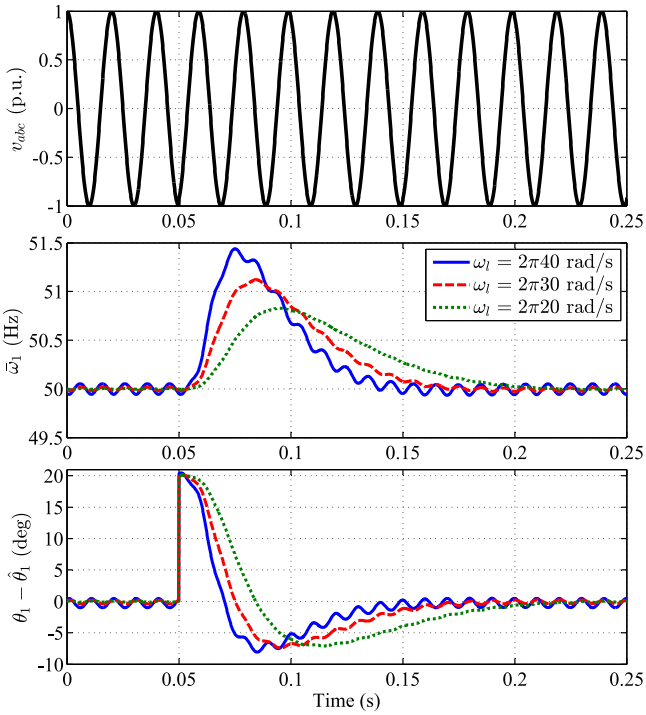

Fig. 14. Simulation results of a pPLL with an IF [see Fig. 13(a)] under a 20° phase jump test. The IF is a third-order butterworth LPF with the cutoff frequency ω_l. Three different values for ω_l is considered. For each value, the proportional and integral gains k_p and k_i are calculated using (25).

$$k_i = \frac{1}{b^3\tau^2} = \frac{\omega_l^2}{4b^3}. \tag{25}$$

Recall that the IF in a pPLL is mainly responsible to filter the double-frequency disturbance term. Therefore, the cutoff frequency ω_l should be sufficiently lower than $2\omega_n = 2\pi 100$ rad/s. The cutoff frequency, however, cannot be reduced too much as it makes the dynamic response very slow. The simulation results in Fig. 14 confirm this idea. Therefore, in selecting ω_l, a tradeoff decision between the speed of dynamic response and the filtering of double-frequency disturbance terms needs to be made. Note that a higher order IIR LPF or another type of IF may be used if a satisfactory compromise cannot be reached.

B. Quadrature Signal Generation-Based PLLs

Another trend in designing advanced 1ϕ PLLs is to use a QSG to virtually create an orthogonal signal from the 1ϕ input signal v and use it as the β-axis input signal of the PLL [2], [32], [33], [34], [35]. Such an orthogonal signal should have the same amplitude as the fundamental component of the input signal v with 90° phase difference. QSG-PLLs differ primarily in how this orthogonal signal is generated. The block diagram representation of a generic QSG-PLL is observed in Fig. 15(a).

The input–output relationship of the QSG in Fig. 15(a) can be described as

$$\begin{bmatrix} \hat{v}_{\alpha,1} \\ \hat{v}_{\beta,1} \end{bmatrix} = \begin{bmatrix} G_\alpha(\rho) \\ G_\beta(\rho) \end{bmatrix} v \tag{26}$$

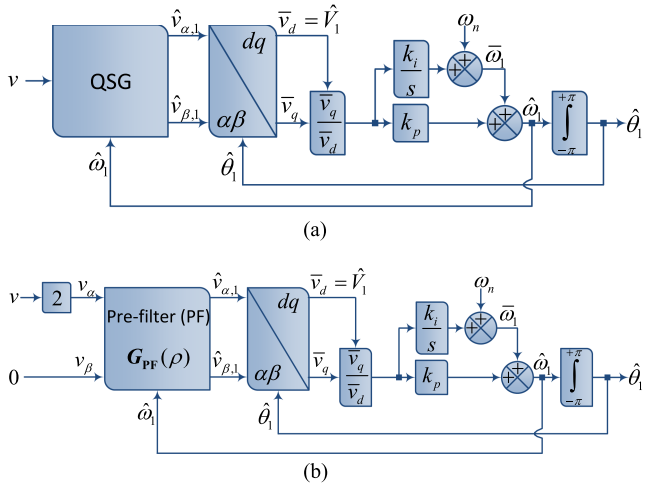

Fig. 15. (a) QSG-PLL. (b) Its alternative representation. The QSG and its corresponding PF are mathematically described by (26) and (28), respectively.

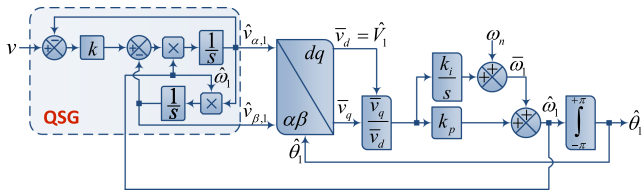

Fig. 16. 1ϕ SOGI-PLL.

which corresponds to

$$\begin{bmatrix} \hat{v}_{\alpha,1} \\ \hat{v}_{\beta,1} \end{bmatrix} = \begin{bmatrix} G_\alpha(\rho) & -G_\beta(\rho) \\ G_\beta(\rho) & G_\alpha(\rho) \end{bmatrix} \begin{bmatrix} v \\ 0 \end{bmatrix} \tag{27}$$

or equivalently

$$\hat{v}_{\alpha,1} + j\hat{v}_{\beta,1} = \underbrace{0.5\left[G_\alpha(\rho) + jG_\beta(\rho)\right]}_{\boldsymbol{G_{PF}}(\rho)} \underbrace{[2v + j0]}_{v_\alpha + jv_\beta}. \tag{28}$$

The abovementioned relationship suggests that a QSG-PLL mathematically corresponds to a standard PLL with a PF, as shown in Fig. 15(b). Therefore, the same tuning procedure presented in Section III is applicable to design the control parameters of QSG-PLLs. Note that $v_\beta = 0$ means that the two-phase input signals v_α and v_β in Fig. 15(b) are imbalanced [see (29)]

$$\begin{aligned} v_\alpha &= 2v = 2V_1\cos(\theta_1) \\ v_\beta &= 0 \end{aligned} \quad \Rightarrow \quad \begin{aligned} v_\alpha &= V_1\cos(\theta_1) + V_1\cos(-\theta_1) \\ v_\beta &= \underbrace{V_1\sin(\theta_1)}_{\text{positive seq.}} + \underbrace{V_1\sin(-\theta_1)}_{\text{negative seq.}} \end{aligned}. \tag{29}$$

The negative-sequence component, however, is blocked in the steady state. This conclusion is based on the fact that the two-phase output signals of the QSG in Fig. 15(a) and, therefore the PF in Fig. 15(b), have the same amplitude with 90° phase difference. It implies that the voltage imbalance of v_α and v_β in Fig. 15(b) can be disregarded during the tuning procedure.

To clarify the abovementioned idea, the PLL in Fig. 16, which is a 1ϕ SOGI-PLL, is considered as the case study. The input–output relationship of the QSG of this PLL can be described as

$$\begin{aligned}\hat{v}_{\alpha,1} &= \overbrace{\frac{k\hat{\omega}_1\rho}{\rho^2+k\hat{\omega}_1\rho+\hat{\omega}_1^2}}^{G_\alpha(\rho)} v \\ \hat{v}_{\beta,1} &= \underbrace{\frac{k\hat{\omega}_1^2}{\rho^2+k\hat{\omega}_1\rho+\hat{\omega}_1^2}}_{G_\beta(\rho)} v\end{aligned} \tag{30}$$

which corresponds to

$$\hat{v}_{\alpha,1}+j\hat{v}_{\beta,1} = \underbrace{\frac{0.5k\hat{\omega}_1(\rho+j\hat{\omega}_1)}{\rho^2+k\hat{\omega}_1\rho+\hat{\omega}_1^2}}_{\boldsymbol{G_{PF}}(\rho)} \underbrace{[2v+j0]}_{v_\alpha+jv_\beta}. \tag{31}$$

If the voltage imbalance of the input two-phase quantities is disregarded, the abovementioned relationship would be the same as the input–output relationship of the DSOGI-PLL's PF [see (13)]. Therefore, the control parameters of the 1ϕ SOGI-PLL can be tuned using the same procedure outlined in Section III-B. The effect of the neglected voltage imbalance can be investigated at the end by developing a linear time-periodic (LTP) model for the 1ϕ SOGI-PLL. Interested readers are referred to [36] for detailed information about the LTP modeling of single-phase SOGI-based grid synchronization systems.

V. Type-3 Synchronization Systems

Admittedly, type-3 synchronization systems are not as popular and common as type-2 ones. However, because of their distinctive feature, which is the ability to track frequency ramps with a zero phase error, many type-3 synchronization systems based on the PLL, FLL, fixed-gain filter, and Kalman filter concepts, among others, have been proposed in the literature [37], [38], [39], [40], [41], [42]. This section mainly aims to demonstrate that the ESO tuning rule is applicable to design the control parameters of type-3 synchronization systems. For the sake of brevity, just type-3 PLLs are studied here.

A. Standard Type-3 PLL (ST3-PLL)

Fig. 17(a) shows an ST3-PLL, in which ω_l, k_p, k_i, and k_a are its control parameters. Throughout this section $\omega_l = k_p$ is considered. In the following, it is shown how the ESO tuning rule [see (5)] may be applied to design the control parameters of the ST3-PLL. This procedure is then extended to more advanced type-3 PLLs.

The linearized model of the ST3-PLL can be readily obtained, as depicted in Fig. 17(b). Using this model, we get

$$G_{ol}^{\theta_1}(s) = \frac{\Delta\hat{\theta}_1(s)}{\Delta\theta_1(s)-\Delta\hat{\theta}_1(s)} = \frac{k_p s^2+k_i s+k_a}{s^3} \tag{32}$$

which is the open-loop TF of the PEL. Obviously, the ESO tuning rule described in Section II is not directly applicable here as it is for control systems having an open-loop TF as (1). However, if we consider the frequency estimation loop (FEL) instead of the PEL, we get

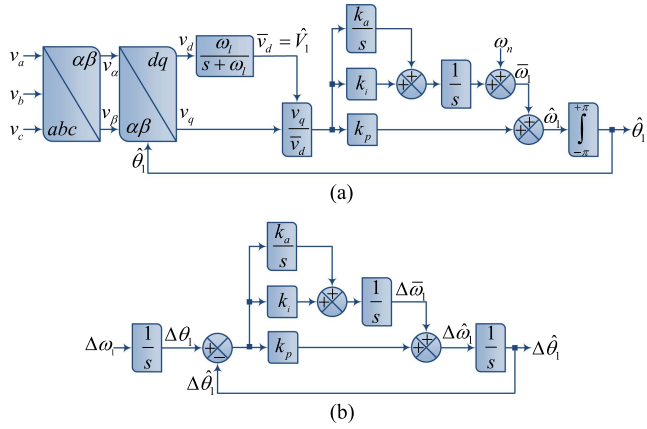

Fig. 17. (a) ST3-PLL. (b) Its LTI model. ω_l, k_p, k_i, and k_a are the control parameters.

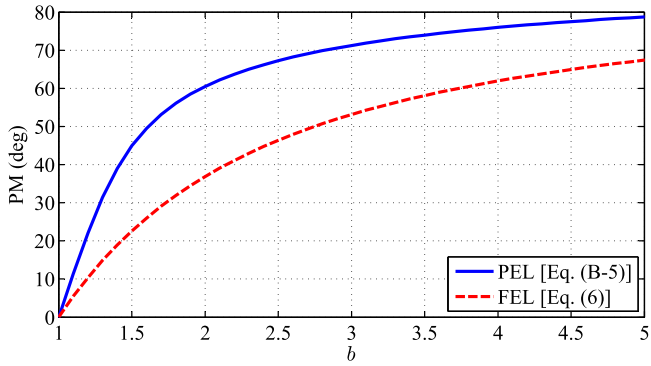

Fig. 18. PMs of the PEL and FEL of the ST3-PLL in Fig. 17 as function of the design constant b.

$$G_{ol}^{\omega_1}(s) = \frac{\Delta\bar{\omega}_1(s)}{\Delta\omega_1(s)-\Delta\bar{\omega}_1(s)} = \frac{k_i s+k_a}{s^2(s+k_p)} = \frac{\overbrace{k_i}^{k}(s+\overbrace{k_a/k_i}^{\omega_z})}{s^2(s+\underbrace{k_p}_{\omega_p})} \tag{33}$$

which is the same as (1). Therefore, the control parameters can be designed using the ESO tuning rule [see (5)] as

$$\begin{aligned}k_p &= \omega_p = b\omega_c \\ k_i &= k = b\omega_c^2 \\ k_a &= k_i\omega_z = \omega_c^3.\end{aligned} \tag{34}$$

As mentioned before [see (6)], the parameter b determines the PM as $\mathrm{PM} = \tan^{-1}(\frac{b^2-1}{2b})$. Note that it is the PM of the FEL here. A natural question arises here: what about the PM of the PEL? It is shown in Appendix B that the PEL's PM, such as the FEL's PM, is solely determined by the design constant b [see (B-5) and (B-6) in the Appendix B]. Therefore, one should design this parameter so that both the PEL and FEL have a good PM. The variations of the PM of both these loops can be observed in Fig. 18. Interestingly, the PEL has always a larger PM than the FEL.

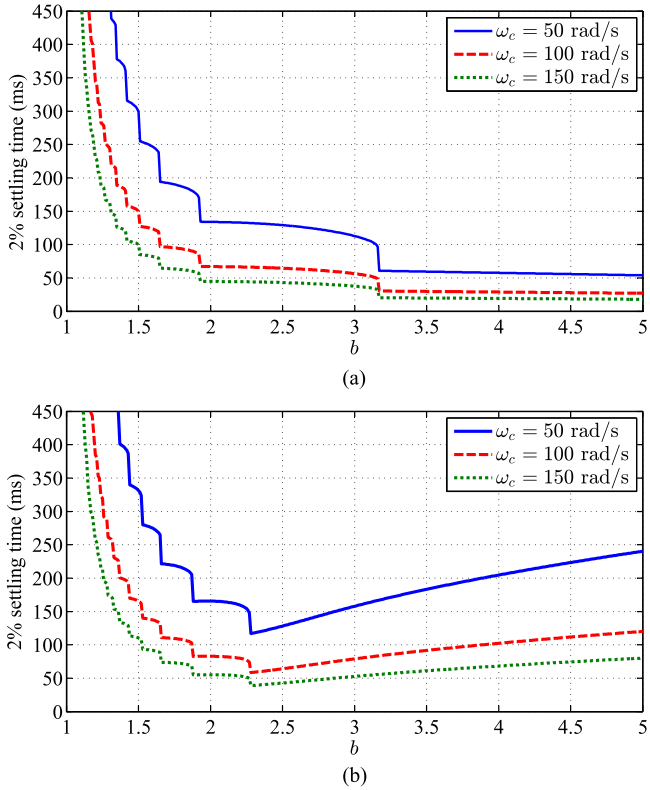

Fig. 19. Variations of the 2% settling time of (a) PEL and (b) FEL of the ST3-PLL as a function of b.

Using (B-1), the closed-loop TF of the PEL can be obtained as

$$G_{cl}^{\theta_1}(s) = \frac{\Delta\hat{\theta}_1(s)}{\Delta\theta_1(s)} = \frac{b\omega_c s^2 + b\omega_c^2 s + \omega_c^3}{s^3 + b\omega_c s^2 + b\omega_c^2 s + \omega_c^3}$$
$$= b\omega_c \frac{\left(s + \frac{\omega_c}{2}\left[1 + \sqrt{1 - 4/b}\right]\right)\left(s + \frac{\omega_c}{2}\left[1 - \sqrt{1 - 4/b}\right]\right)}{(s + \omega_c)(s^2 + (b-1)\omega_c s + \omega_c^2)}. \quad (35)$$

Based on the abovementioned TF, which has three poles and two zeros, the following observations can be made.

1) A closed-loop pole is located at $s = -\omega_c$.
2) For two other poles, the damping factor and the natural frequency are equal to $(b-1)/2$ and ω_c, respectively. It means that $b < 3$ ($b \geq 3$) results in a pair of complex-conjugate (real) poles. Note that $b = 3$ leads to two coincident poles at $s = -\omega_c$, and $b = 1 + \sqrt{2}$ results in a pair of complex-conjugate poles with the damping factor $1/\sqrt{2}$.
3) Two zeros are complex-conjugate (real) if $b < 4$ ($b \geq 4$). Note that $b = 4$ results in two coincident zeros at $s = -\omega_c/2$.

The abovementioned information suggests that a reasonable range for the design constant b could be $1 + \sqrt{2} \leq b \leq 4$. To make this range narrower, some investigations are conducted in the following.

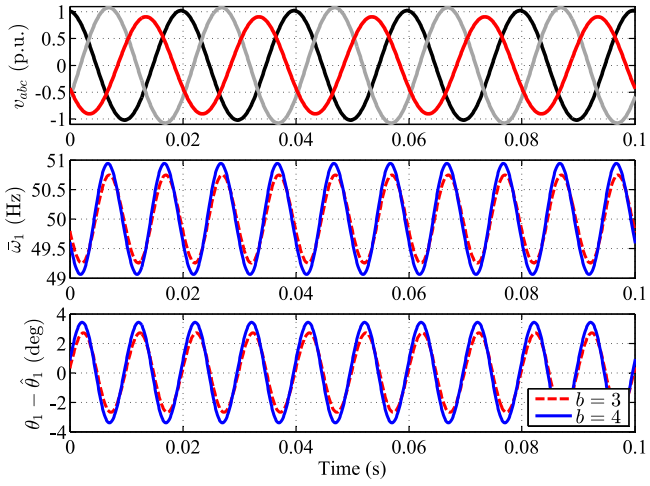

Fig. 20. Effect of the design constant b on the filtering capability of the ST3-PLL. The grid voltage is imbalanced and without harmonic distortion. $\omega_c = 100$ rad/s is selected. For each value of b, the parameters k_p k_i, and k_a are calculated using (34). The sampling frequency is 10 kHz.

In Fig. 19(a), the variations of the 2% settling time of the PEL as a function of b and ω_c are observed. This settling time denotes the time required for the phase error signal $\theta_1 - \hat{\theta}_1$ to reach and stay within the 2% tolerance band around zero after a phase jump. As can be seen, increasing both b and ω_c reduces the settling time. However, this reduction is negligible for $b > 3.2$ (for a given value of ω_c). Therefore, $b = 3.2$ could be a good choice to minimize the phase error settling time after a phase jump. This value results in a PM equal to 55.3° and 72.4° for the FEL and PEL of the ST3-PLL, respectively. Note that noise immunity is an issue that prevents excessive increases in the parameter b. To be more exact, for a given ω_c, increasing the parameter b may reduce the noise immunity of the ST3-PLL. The numerical results in Fig. 20 confirm this fact. Note that the magnitude of oscillatory errors at the output of the ST3-PLL increases with increasing b. Besides, as discussed in the following, increasing the parameter b may adversely affect the frequency tracking speed of the ST3-PLL

Fig. 19(b) shows the variations of the 2% settling time of the FEL as a function of b and ω_c. Note that this settling time refers to the time required for the estimated frequency $\hat{\omega}_1$ to reach and stay within the 2% tolerance band around the actual frequency ω_1 after a frequency jump. It is observed that, regardless of the value of ω_c, the settling time is minimized around $b = 1 + \sqrt{2}$. This value leads to a PM around 45° and 66.4° for the FEL and PEL of the ST3-PLL, respectively.

Based on the abovementioned study, $1 + \sqrt{2} \leq b \leq 3.2$ is recommended for designing the control parameters of the ST3-PLL. In this range, $b = 3.2$ is probably an optimum choice in most practical scenarios because it minimizes the settling time of the ST3-PLL after phase jumps and maximizes its PM. Note that frequency jumps are not expected in power systems. Note also that an increased PM results in a more smooth dynamic response with a lower overshoot.

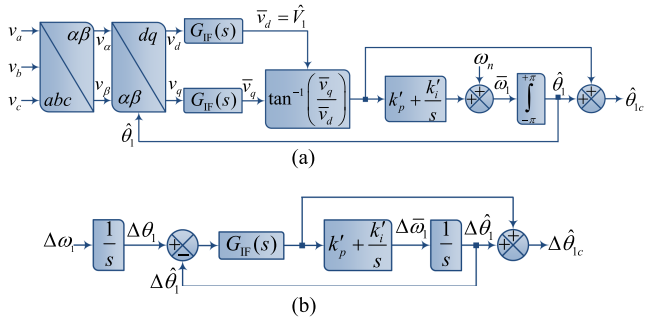

Fig. 21. (a) QT2-PLL. (b) Its LTI model.

Regarding the gain crossover frequency ω_c, one should note that increasing this parameter increases the bandwidth (and therefore the speed of response) and reduces the noise immunity. Therefore, one has to make a tradeoff decision based on the application requirements and priorities.

B. Advanced Type-3 PLLs

Advanced type-3 PLLs often look quite different than the standard one in Fig. 17(a) and may be even presumed a type-2 PLL at first glance. For instance, consider the PLL in Fig. 21(a). It is called the quasi type-2 PLL (QT2-PLL) because it looks like a type-2 PLL, but it is actually a type-3 PLL. Deriving the QT2-PLL is inspired by the quasi type-1 PLL (QT1-PLL) presented in [43]. A similar PLL to the QT2-PLL, called the ZPLL, is presented in [42].

First, we need to show that the QT2-PLL is actually a type-3 control system. To this end, the linearized model of the QT2-PLL is needed. This model can be simply obtained, as shown in Fig. 21(b). Using this model, the open-loop TF of the PEL can be obtained as

$$G_{ol}^{\theta_1}(s)=\frac{\Delta\hat{\theta}_{1c}(s)}{\Delta\theta_1(s)-\Delta\hat{\theta}_{1c}(s)}=\frac{G_{\rm IF}(s)}{1-G_{\rm IF}(s)}\frac{s^2+k_p's+k_i'}{s^2} \tag{36}$$

where, $G_{\rm IF}$ is an IF, e.g., an n-order IIR LPF, a chain of IIR NFs, a chain of *dq*DSC operators, or an MAF, among others. In Table I, it was shown that all these filters can be well-approximated by a first-order lag filter at low frequencies. If we substitute $G_{\rm IF}(s)\approx\frac{1}{\tau s+1}$ in (36), we get

$$G_{ol}^{\theta_1}(s)\approx\frac{\overbrace{(1/\tau)}^{k_p}s^2+\overbrace{(k_p'/\tau)}^{k_i}s+\overbrace{(k_i'/\tau)}^{k_a}}{s^3}. \tag{37}$$

The abovementioned equation shows that the PEL of the QT2-PLL has three open-loop poles at the origin. Therefore, the QT2-PLL is a type-3 PLL. Note that the abovementioned approximation is accurate in a low-frequency range. This range is mainly determined by the bandwidth of $G_{\rm IF}(s)$.

The similarity between (32) and (37) suggests that the QT2-PLL and the ST3-PLL are equivalent in the low-frequency range from a small-signal perspective if their control parameters meet the following condition:

$$\begin{aligned}1/\tau&=k_p\\ k_p'/\tau&=k_i\\ k_i'/\tau&=k_a.\end{aligned} \tag{38}$$

In (34), an ESO-based rule for tuning the control parameters of the ST3-PLL was presented. Based on this tuning rule and the equivalence condition (38), we may obtain a rule for tuning the control parameters of the QT2-PLL as

$$\begin{aligned}1/\tau&=b\omega_c\\ k_p'/\tau&=b\omega_c^2\\ k_i'/\tau&=\omega_c^3\end{aligned}\quad\Rightarrow\quad\begin{aligned}\tau&=1/(b\omega_c)\\ k_p'&=\omega_c\\ k_i'&=\omega_c^2/b.\end{aligned} \tag{39}$$

If due to some constraints and/or design considerations the time constant τ is already fixed, the abovementioned tuning rule can be rewritten as

$$\begin{aligned}k_p'&=\tfrac{1}{b\tau}\\ k_i'&=\tfrac{1}{b^3\tau^2}.\end{aligned} \tag{40}$$

1) Design Example: Assume that $G_{\rm IF}(s)$ in Fig. 21(a) is an MAF, i.e., $G_{\rm IF}(s)=\frac{1-e^{-T_w s}}{T_w s}$, where T_w is its window length. Designing the MAF's window length in PLL applications has been well-discussed in [11]. According to [11], a good choice is to set the window length equal to half the grid fundamental period, i.e., $T_w=0.01$ s in a 50 Hz system, as it enables the PLL to block (or at least significantly attenuate) the grid voltage imbalance and all odd-order harmonics of the grid voltage.

In Table I, it was shown that the MAF's TF can be approximated as $G_{\rm IF}(s)=\frac{1-e^{-T_w s}}{T_w s}\approx\underbrace{\frac{1}{(T_w/2)}}_{\tau}\frac{1}{s+1}$. With the selection $T_w=0.01$ s, we get $\tau=T_w/2=0.005$ s. To minimize the phase jump settling time and ensure a high stability margin, as discussed in the previous section, $b=3.2$ is selected. With $\tau=0.005$ s and $b=3.2$, the proportional and integral gains of the QT2-PLL are determined according to (40) as $k_p'=62.5$ and $k_i'=1220.7$.

2) Comparison: In this section, a comparison between the QT2-PLL designed in the previous section and the ST3-PLL is carried out. The control parameters of the QT2-PLL are $T_w=0.01$ s (which corresponds to $\tau=0.005$ s), $k_p'=62.5$ and $k_i'=1220.7$. To have a fair comparison, the control parameters of the ST3-PLL are calculated according to (38), which gives $k_p=200$, $k_i=12500$, and $k_a=244140$.

In Fig. 22, the open-loop frequency response of the PEL of the QT2-PLL and ST3-PLL is observed. Based on these plots, the following observations are made.

a) Both PLLs have a close frequency response at low frequencies. It implies that they will represent a close dynamic behavior in response to phase jumps, frequency jumps, frequency ramps, etc. The dynamic response of the TS3-PLL is expected to be slightly more damped as it has a higher PM. The numerical results in Fig. 23(a) confirm these predictions.

b) Thanks to the action of the MAFs in its structure, which results in notches in its frequency response, the QT2-PLL

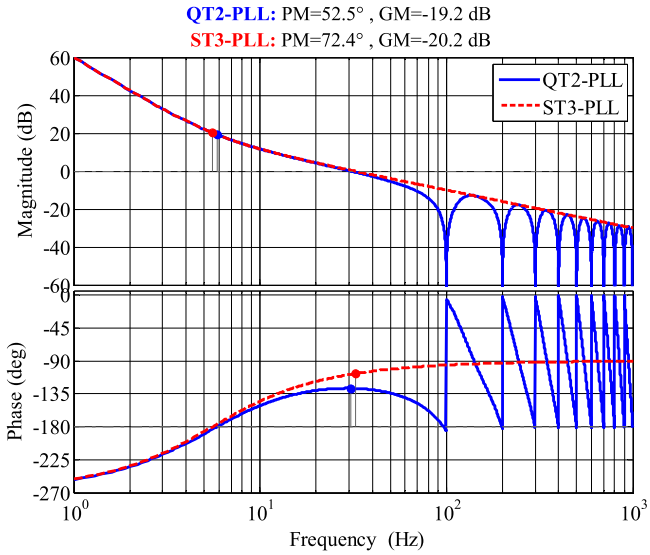

Fig. 22. Open-loop frequency response of the PEL of the QT2-PLL and ST3-PLL.

offers a higher filtering capability than the ST3-PLL, especially when the grid frequency is at or close to its nominal value. The numerical results in Fig. 23(b) support these conclusions. Note that the MAFs used in the QT2-PLL are nonadaptive. Therefore, they cannot completely block the grid voltage imbalance/harmonics under off-nominal frequencies.

3) Problematic Filters: Using some types of filters in the QT2-PLL structure may be problematic. This section aims to highlight this fact.

Using (36), the closed-loop TF of the PEL of the QT2-PLL can be obtained as

$$G_{cl}^{\theta_1}(s) = \frac{G_{ol}^{\theta_1}(s)}{1 + G_{ol}^{\theta_1}(s)} = \frac{G_{\mathrm{IF}}(s)\left(s^2 + k_p' s + k_i'\right)}{s^2 + G_{\mathrm{IF}}(s)\left(k_p' s + k_i'\right)}. \quad (41)$$

In [42], a single *dq*DSC operator whose TF is $G_{\mathrm{IF}}(s) = 0.5(1 + e^{-\frac{T}{4}s})$ is suggested as the IF. Bode plots of this filter and the abovementioned closed-loop TF are observed in Fig. 24. These plots show that the filtering capability of the QT2-PLL relies heavily on its IF. Therefore, a poor IF design leads to poor noise immunity for the QT2-PLL. For example, it is observed in Fig. 24 that the designed IF makes $|G_{cl}^{\theta_1}(j\omega)| = 0$ dB at 200 Hz and its integer multiples, which means the QT2-PLL cannot filter their corresponding disturbance components.

In summary, the QT2-PLL mainly relies on its IF to filter grid voltage disturbances. Therefore, the IF should be designed wisely to ensure good noise immunity.

VI. Frequency-Locked Loops

In the grid synchronization context, an FLL is a nonlinear recursive filter equipped with a frequency observer to adapt it to grid frequency changes. Similar to PLLs, advanced FLLs are often developed by including a PF or IF into some basic FLL structures. For instance, Fig. 25(a) shows a basic 3ϕ FLL[1] with a PF and Fig. 26(a) illustrates the same FLL with an IF [5], [7], [8], [9]. The ESO tuning rule is applicable for tuning the control parameters of these FLLs. However, they need to be transformed into their corresponding PLL structures first.

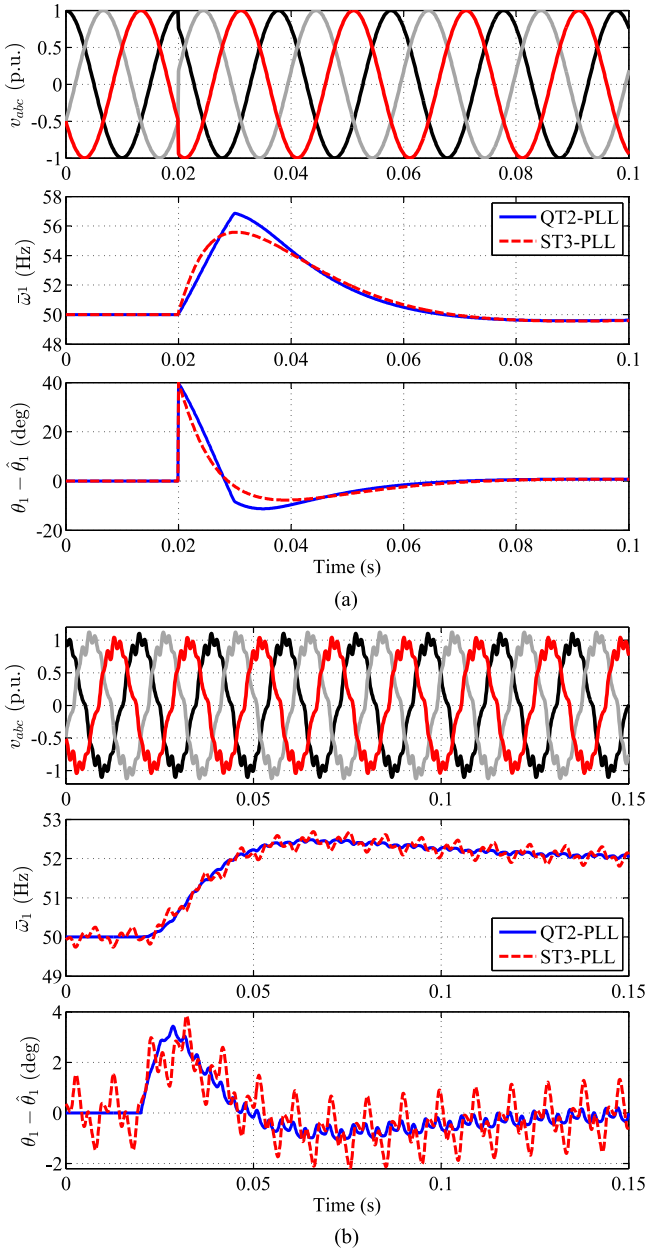

Fig. 23. Numerical comparison between the QT2-PLL and ST3-PLL under (a) a 40° phase jump test and (b) an imbalanced ($V_{-1} = 0.05$ p.u.) and harmonically distorted ($V_{-5} = V_{+7} = V_{-11} = V_{+13} = 0.05$ p.u.) grid condition with a +2-Hz frequency jump. The control parameters of the ST3-PLL are $k_p = \omega_l = 200$, $k_i = 12500$, and $k_a = 244140$. The control parameters of the QT2-PLL are $T_w = 0.01$ s, $k_p' = 62.5$, and $k_i' = 1220.7$. The sampling frequency is 10 kHz.

[1]It is often called the reduced-order generalized integrator-based FLL (ROGI-FLL) or the complex band pass filter FLL (CBF-FLL) in the literature [7], [8], [9], [10].

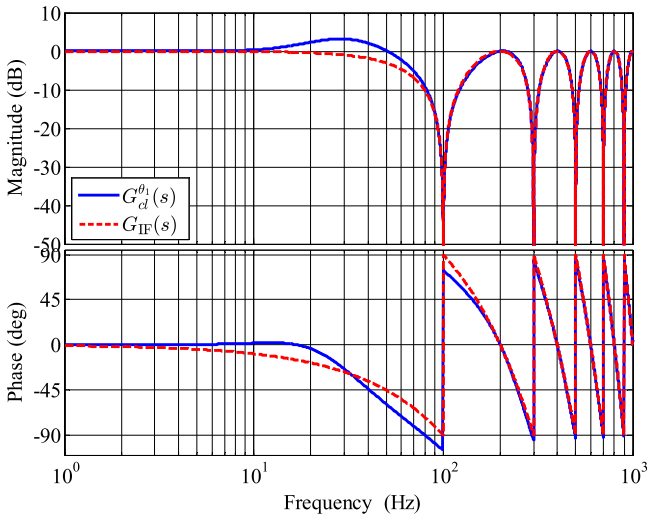

Fig. 24. Bode plots of $G_{\rm IF}(s) = 0.5(1 + e^{-\frac{T}{4}s})$ and the closed-loop TF (41). The control gains are $k_p' = 165.68$ and $k_i' = 11370.85$ [42].

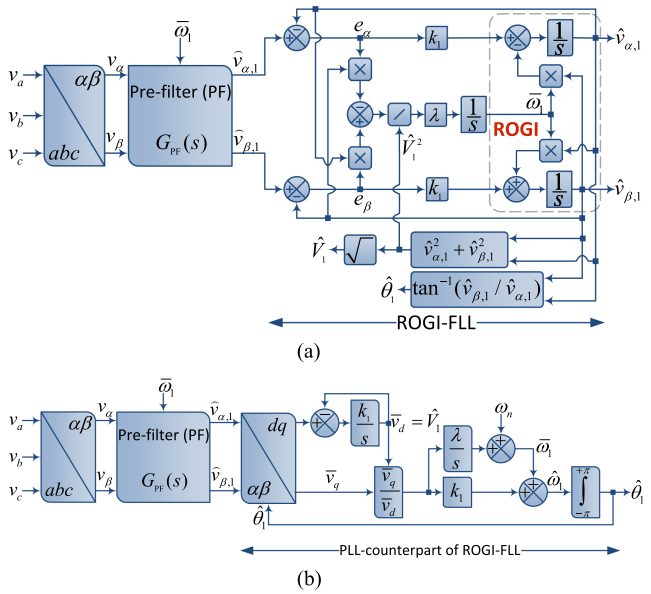

Fig. 25. (a) Basic 3ϕ FLL with PF. (b) Its PLL counterpart.

To better understand the abovementioned idea, consider the ROGI-FLL in Fig. 27(a) and the PLLs in Fig. 27(b) and (c). All these synchronization systems have the same governing nonlinear differential equations (GNDEs) as [7], [8]

$$\begin{aligned}\dot{\hat{\theta}}_1 &= \bar{\omega}_1 + \frac{k_1}{\hat{V}_1}\Big(-\sin(\hat{\theta}_1)v_\alpha + \cos(\hat{\theta}_1)v_\beta\Big)\\ \dot{\bar{\omega}}_1 &= \frac{\lambda}{\hat{V}_1}\Big(-\sin(\hat{\theta}_1)v_\alpha + \cos(\hat{\theta}_1)v_\beta\Big)\\ \dot{\hat{V}}_1 &= k_1\Big(\cos(\hat{\theta}_1)v_\alpha + \sin(\hat{\theta}_1)v_\beta - \hat{V}_1\Big).\end{aligned} \tag{42}$$

It implies that they are all mathematically equivalent. If we replace the ROGI-FLL in Fig. 25(a) with its equivalent PLL

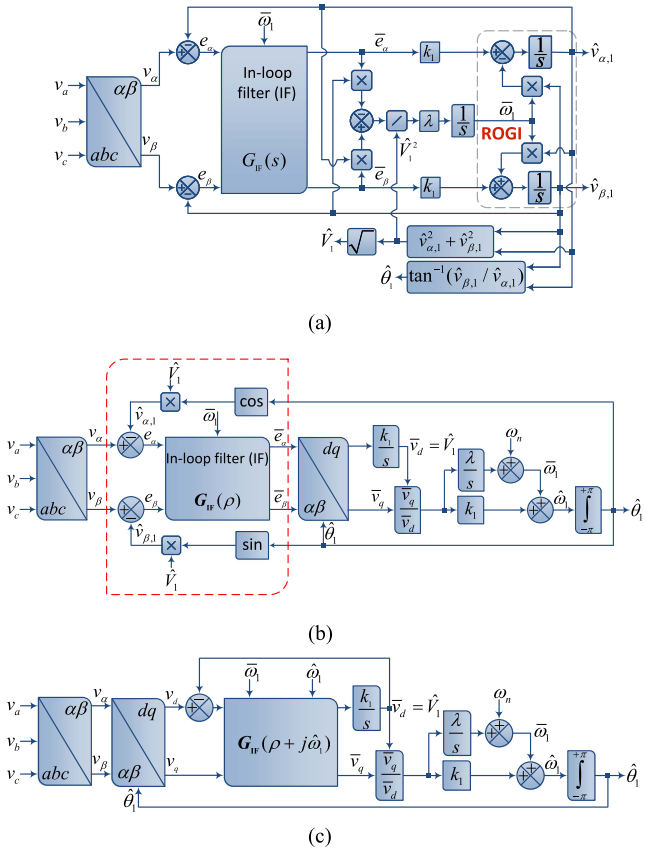

Fig. 26. (a) Basic 3ϕ FLL with IF. (b) and (c) Its PLL counterpart.

in Fig. 27(b), we get Fig. 25(b), which is a standard 3ϕ PLL with a PF. Therefore, the same design procedure presented in Section III can be used for tuning the control parameters.

In a similar manner, if we replace the ROGI-FLL in Fig. 26(a) with its equivalent PLL in Fig. 27(c), we get Fig. 26(b). If we transfer the dashed box in Fig. 26(b) to the *dq* frame, we get Fig. 26(c), which is a standard 3ϕ PLL with an IF. Therefore, the tuning procedure presented in Section II-B can be deployed for tuning the control parameters.

As a case study, consider Fig. 28(a), which is a basic FLL equipped with a first-order complex-band-pass filter (CBF) as the IF. Considering the abovementioned discussions, the PLL counterpart of this FLL can be readily obtained, as shown in Fig. 28(b). From a small-signal perspective, the *dq*-axis cross-coupling in the dashed box in Fig. 28(b) has a negligible effect. Therefore, the PLL in Fig. 28(b) can be well-approximated by that in Fig. 28(c). The LTI model of this PLL is shown in Fig. 28(d). The open-loop TF of the PEL of this model is

$$G_{ol}^{\theta_1}(s) = \frac{k_2}{s+k_2}\frac{k_1 s+\lambda}{s^2} = \frac{\overbrace{(k_1k_2)}^{k}(s+\overbrace{\lambda/k_1}^{\omega_z})}{s^2(s+\underbrace{k_2}_{\omega_p})}. \tag{43}$$

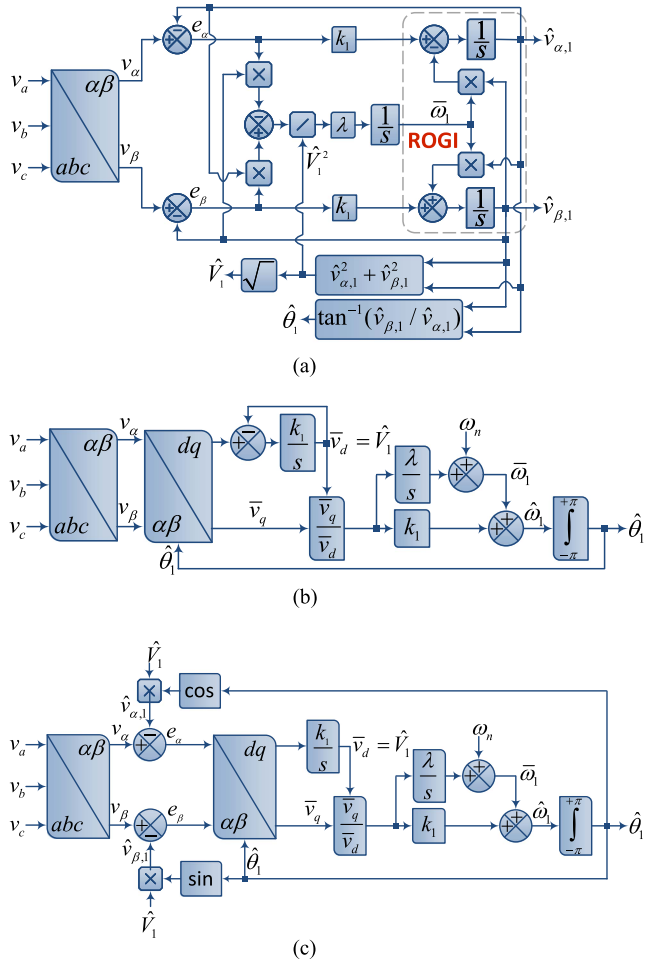

Fig. 27. (a) ROGI-FLL. (b) and (c) Its corresponding PLLs.

Therefore, according to the ESO tuning rule in (5), the control parameters can be designed as

$$\begin{aligned} k_1 &= \omega_c \\ k_2 &= b\omega_c \\ \lambda &= \omega_c^2/b \end{aligned} \tag{44}$$

VII. Limitations of a High-Bandwidth Control Design

Sometimes, the ESO tuning rule may not be as efficient as expected. The reason is that this tuning method is often based on a reduced-order LTI model of grid synchronization systems, which neglects the presence of grid voltage disturbances and/or the high-frequency dynamics of IFs or PFs. This issue may lead to lower stability margins than promised (targeted) values or may even cause some stability issues. An example makes this fact easier to understand. In Section III-B, we presented (18) for designing the control parameters of the DSOGI-PLL. Recall that deriving (18) was based on a simplified (reduced-order) IF-form representation of the DSOGI-PLL [see Fig. 8(b)]. Recall also that we neglected the presence of any disturbance component in the grid voltage during the design procedure. If we calculate k_p and k_i according to (18), the reduced-order LTI model in Fig. 9

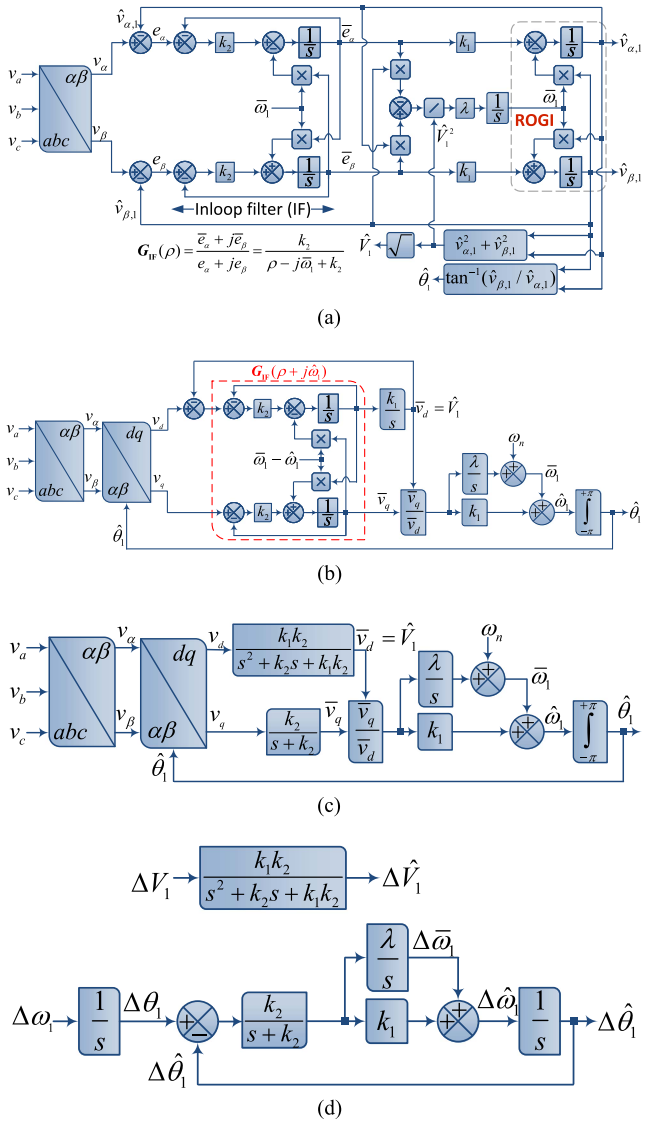

Fig. 28. (a) Basic FLL equipped with a first-order complex-band-pass filter as the IF. (b) and (c) Its PLL counterparts. (d) Its LTI model.

predicts that the DSOGI-PLL achieves a fixed stability margin as long as b is constant. For instance, it predicts $\mathrm{PM}_1 = 45°$, $\mathrm{PM}_2 = 90°$, and $\mathrm{GM}_1 = \mathrm{GM}_2 = \inf$ if $b = 1 + \sqrt{2}$ is selected (see Fig. 10). By deriving more accurate linear models for the DSOGI-PLL, we are going to investigate how a high-bandwidth design and/or the presence of disturbance components in the grid voltage affects the abovementioned predictions. Throughout this study, the proportional and integral gains k_p and k_i are calculated according to (18).

A. High-Bandwidth Design Without Considering Input Disturbance Components

The exact IF-form equivalent of the DSOGI-PLL is the same as Fig. 7(c), where $G_r(\rho)$ and $G_i(\rho)$ are as expressed in (15). If we neglect the presence of disturbance components in the grid voltage and linearize this structure, we get a full-order LTI

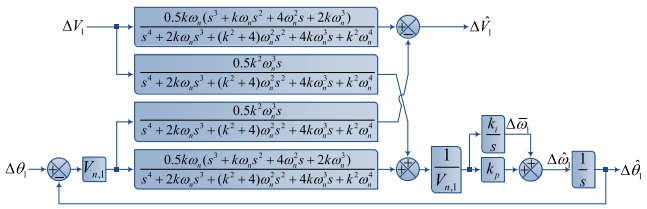

Fig. 29. Full-order LTI model of the DSOGI-FLL, which is obtained by linearizing Fig. 7(c). $V_{n,1}$ is the nominal value of the fundamental positive-sequence component of v_{abc}.

TABLE III
DSOGI-PLL'S STABILITY MARGINS PREDICTED BY ITS FULL-ORDER LTI MODEL FOR DIFFERENT SETS OF CONTROL PARAMETERS

Stability margins	Control parameters: $b = 1+\sqrt{2}$, $k_p = \frac{k\omega_n}{2b}$, $k_i = \frac{k^2\omega_n^2}{4b^3}$			
	$k = \sqrt{2}$	$k = 2$	$k = 2.5$	$k = 3$
PM_1	$\approx 44.4°$	$\approx 43°$	$\approx 36.9°$	$\approx 20.7°$
PM_2	$\approx 81°$	$\approx 75.9°$	$\approx 75.1°$	$\approx 77.2°$
GM_1	≈ 18 dB	≈ 11.5 dB	≈ 7.5 dB	≈ 4.3 dB
GM_2	Inf	Inf	Inf	Inf

model, as shown in Fig. 29. With this model, the open-loop transfer matrix of the DSOGI-PLL can be obtained as expressed in (45) shown at the bottom of this page. Using (45), we may obtain the open-loop eigenloci of the DSOGI-PLL and measure its stability margins. For instance, Fig. 30(a) shows the open-loop eigenloci of the DSOGI-PLL and its stability margins for the same control parameters designed in Section III-B. Note that we get two eigenvalue PMs ($\mathrm{PM}_1 \approx 44.4°$ and $\mathrm{PM}_2 \approx 81°$) and two eigenvalue GMs ($\mathrm{GM}_1 \approx 18$ dB and $\mathrm{GM}_2 = \mathrm{inf}$) because the LTI model of the DSOGI-PLL (see Fig. 29) is a TITO system. These stability margins are close to those predicted before using the reduced-order model of the DSOGI-PLL (see Fig. 10) because a rather low-bandwidth design was considered in Section III-B.

Now, let us increase the DSOGI-PLL's bandwidth. Fig. 30(b)–(d) show open-loop eigenloci of the DSOGI-PLL for $k = 2$, 2.5, and 3. Note that in all these cases, b is fixed to $1+\sqrt{2}$, and k_p and k_i are calculated using (18). Based on the results in Fig. 30(b)–(d), the following observations can be made.

1) By increasing the SOGI gain k, which corresponds to increasing the DSOGI-PLL's bandwidth, the stability margins are reduced (see Table III for details). This observation is not consistent with the predictions made in Section III-B as they are based on the reduced-order LTI model in Fig. 9, which is not very accurate at high frequencies.
2) Roughly speaking, the reduction rate of stability margins increases with the DSOGI-PLL's bandwidth. Fig. 31, which shows the variation of PM_1 as a function of the SOGI gain k helps to better visualize this fact. This plot predicts that $k > 3.88$ leads to a negative PM and, therefore, an unstable condition.

To verify the abovementioned theoretical prediction, a numerical test on the DSOGI-PLL [see Fig. 8(a)] is performed in MATLAB/Simulink environment. Initially, the SOGI gain k is set to 3.8. At $t = 0.5$ s, the value of this gain is suddenly increased to 3.9. The output frequency of the DSOGI-PLL is shown in Fig. 32. As expected, the DSOGI-PLL is initially stable. However, it becomes unstable after increasing the SOGI gain k.

B. High-Bandwidth Design With Considering Input Disturbance Components

Grid voltage disturbances were not taken into account in the previous section. In this section, an imbalanced grid condition is assumed and its effect on the stability margin of the DSOGI-PLL is investigated. To this end, an LTP model of the DSOGI-PLL is needed. Such a model can be derived by linearizing GNDEs of the DSOGI-PLL around a periodic trajectory [44].

If we consider the $\alpha\beta$-axis input and output signals of the PF of the DSOGI-PLL as (46)–(48), an LTP model, as shown in Fig. 33 can be obtained for the DSOGI-PLL

$$\begin{aligned} v_\alpha(t) &= V_1\cos(\theta_1) + V_{-1}\cos(\theta_{-1}) \\ v_\beta(t) &= V_1\sin(\theta_1) + V_{-1}\sin(\theta_{-1}) \end{aligned} \tag{46}$$

$$\begin{aligned} \hat{v}_{\alpha,1}(t) &= \bar{V}_1\cos(\bar{\theta}_1) \\ \hat{v}_{\beta,1}(t) &= \bar{V}_1\sin(\bar{\theta}_1) \end{aligned} \tag{47}$$

$$\begin{aligned} \hat{v}_{\alpha,-1}(t) &= \bar{V}_{-1}\cos(\bar{\theta}_{-1}) \\ \hat{v}_{\beta,-1}(t) &= \bar{V}_{-1}\sin(\bar{\theta}_{-1}). \end{aligned} \tag{48}$$

Note that to obtain the LTP model, both the actual and estimated parameters are defined as $x_h = x_{n,h} + \Delta x_h$, where the subscript n denotes a working point, the prefix Δ denotes a small perturbation, and the subscript h denotes the order of frequency component. For instance, the fundamental negative-sequence amplitude V_{-1} is defined as $V_{-1} = V_{n,-1} + \Delta V_{-1}$.

Using the obtained LTP model, the open-loop harmonic transfer function (HTF) of the DSOGI-PLL can be obtained as (49) shown at the bottom of the next page, in which

$$\begin{aligned} \boldsymbol{V}_{e,1}^{\mathrm{htf}}(s) &= [\cdots, V_{e,1}(s_{-1}), V_{e,1}(s_0), V_{e,1}(s_{+1}), \cdots]^T \\ \boldsymbol{\theta}_{e,1}^{\mathrm{htf}}(s) &= [\cdots, \theta_{e,1}(s_{-1}), \theta_{e,1}(s_0), \theta_{e,1}(s_{+1}), \cdots]^T \\ \boldsymbol{V}_{e,-1}^{\mathrm{htf}}(s) &= [\cdots, V_{e,-1}(s_{-1}), V_{e,-1}(s_0), V_{e,-1}(s_{+1}), \cdots]^T \\ \boldsymbol{\theta}_{e,-1}^{\mathrm{htf}}(s) &= [\cdots, \theta_{e,-1}(s_{-1}), \theta_{e,-1}(s_0), \theta_{e,-1}(s_{+1}), \cdots]^T \end{aligned}$$

$$\begin{bmatrix} \Delta\hat{V}_1(s) \\ \Delta\hat{\theta}_1(s) \end{bmatrix} = \begin{bmatrix} \frac{k\omega_n\left(s^3+k\omega_n s^2+4\omega_n^2 s+2k\omega_n^3\right)}{2s^4+3\omega_n k s^3+(k^2+8)\omega_n^2 s^2+4k\omega_n^3 s} & -\frac{V_{n,1}k^2\omega_n^3}{2s^3+3\omega_n k s^2+(k^2+8)\omega_n^2 s+4k\omega_n^3} \\ \frac{1}{V_{n,1}}\frac{k^2\omega_n^3(k_p s+k_i)}{2s^5+3k\omega_n s^4+(k^2+8)\omega_n^2 s^3+4k\omega_n^3 s^2} & \frac{0.5k\omega_n\left(2k_p s^3+(k_p k\omega_n+2k_i)s^2+(k_i k\omega_n+8k_p\omega_n^2)s+8k_i\omega_n^2\right)}{2s^5+3k\omega_n s^4+(k^2+8)\omega_n^2 s^3+4k\omega_n^3 s^2} \end{bmatrix} \begin{bmatrix} \Delta V_1(s)-\Delta\hat{V}_1(s) \\ \Delta\theta_1(s)-\Delta\hat{\theta}_1(s) \end{bmatrix}. \tag{45}$$

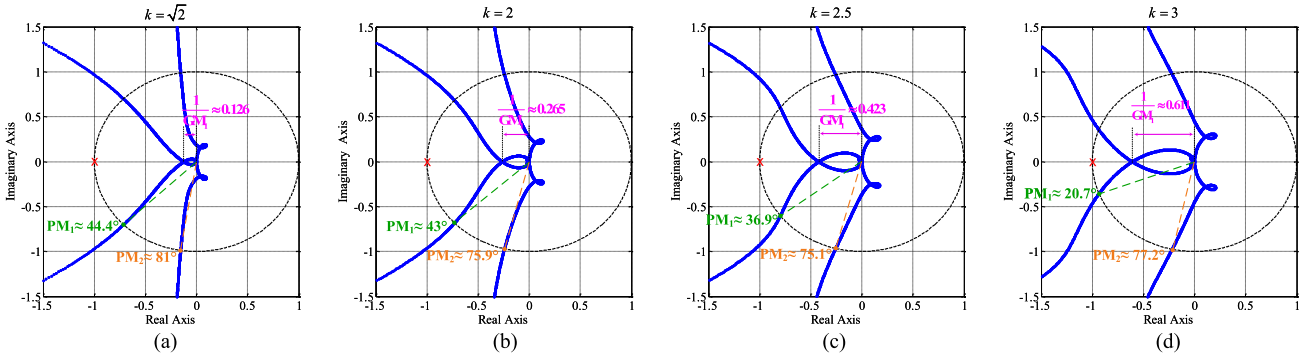

Fig. 30. Open-loop eigenloci of the DSOGI-PLL with different sets of control parameters. (a) $k=\sqrt{2}$. (b) $k=2$. (c) $k=2.5$. (d) $k=3$. In all cases, $b=1+\sqrt{2}$, $\omega_n=2\pi 50$ rad/s, $k_p=\frac{k\omega_n}{2b}$, and $k_i=\frac{k^2\omega_n^2}{4b^3}$ [see (18)].

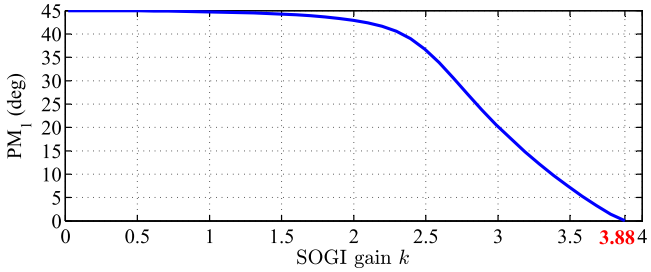

Fig. 31. Variations of an eigenvalue PM of the DSOGI-PLL as a function of the SOGI gain k. The open-loop transfer matrix of the full-order LTI model of the DSOGI-PLL is used for obtaining these results [see Fig. 29 and (45)]. Control parameters are $b=1+\sqrt{2}$, $k_p=\frac{k\omega_n}{2b}$, and $k_i=\frac{k^2\omega_n^2}{4b^3}$.

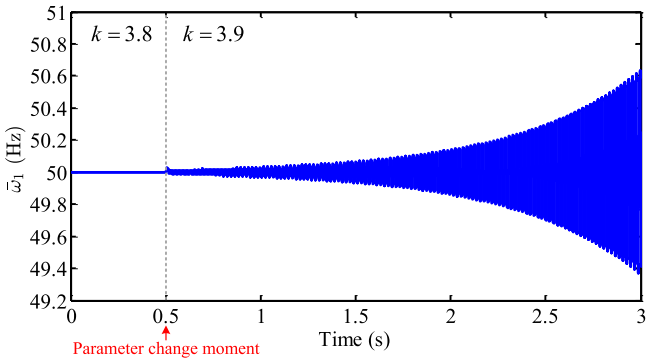

Fig. 32. Numerical verification of the stability range $k<3.88$ of the DSOGI-PLL, which is theoretically predicted in Fig. 31. Control parameters are $b=1+\sqrt{2}$, $k_p=\frac{k\omega_n}{2b}$, and $k_i=\frac{k^2\omega_n^2}{4b^3}$. The sampling frequency is 10 kHz.

$$\Delta\hat{\boldsymbol{V}}_1^{\text{htf}}(s)=[\cdots,\Delta\hat{V}_1(s_{-1}),\Delta\hat{V}_1(s_0),\Delta\hat{V}_1(s_{+1}),\cdots]^T$$
$$\Delta\hat{\boldsymbol{\theta}}_1^{\text{htf}}(s)=[\cdots,\Delta\hat{\theta}_1(s_{-1}),\Delta\hat{\theta}_1(s_0),\Delta\hat{\theta}_1(s_{+1}),\cdots]^T$$
$$\Delta\bar{\boldsymbol{V}}_{-1}^{\text{htf}}(s)=[\cdots,\Delta\bar{V}_{-1}(s_{-1}),\Delta\bar{V}_{-1}(s_0),\Delta\bar{V}_{-1}(s_{+1}),\cdots]^T$$
$$\Delta\bar{\boldsymbol{\theta}}_{-1}^{\text{htf}}(s)=[\cdots,\Delta\bar{\theta}_{-1}(s_{-1}),\Delta\bar{\theta}_{-1}(s_0),\Delta\bar{\theta}_{-1}(s_{+1}),\cdots]^T$$
$$\boldsymbol{G}_x^{\text{htf}}(s)=\text{diag}(\cdots,G_x(s_{-1}),G_x(s_0),G_x(s_{+1}),\cdots)$$
$$\theta_{n,1}-\theta_{n,-1}=(\omega_n t+\varphi_1)-(-\omega_n t+\varphi_{-1})=\underbrace{2\omega_n}_{\omega_{ps}}t+\underbrace{\varphi_1-\varphi_{-1}}_{\varphi_{ps}}$$

$$s_m=s+jm\omega_{ps}\quad(m\in\mathcal{Z})$$
$$G_a(s)=\frac{k\omega_n/2}{s}$$
$$G_b(s)=\frac{k\omega_n/2}{s+k\omega_n/2}\frac{k_p s+k_i}{s^2}$$
$$G_{\text{LPF}}(s)=\frac{k\omega_n/2}{s+k\omega_n/2}$$
$$G_{\text{HPF}}(s)=\frac{s}{s+k\omega_n/2}$$

$$\begin{bmatrix}\Delta\hat{\boldsymbol{V}}_1^{\text{htf}}(s)\\ \Delta\hat{\boldsymbol{\theta}}_1^{\text{htf}}(s)\\ \Delta\bar{\boldsymbol{V}}_{-1}^{\text{htf}}(s)\\ \Delta\bar{\boldsymbol{\theta}}_{-1}^{\text{htf}}(s)\end{bmatrix}=\begin{bmatrix}\boldsymbol{G}_a^{\text{htf}}(s) & \boldsymbol{0} & \boldsymbol{G}_a^{\text{htf}}(s)\boldsymbol{A}_{\cos}^{\text{htf}}\\ \boldsymbol{0} & \boldsymbol{G}_b^{\text{htf}}(s) & \frac{1}{V_{n,1}}\boldsymbol{G}_b^{\text{htf}}(s)\boldsymbol{A}_{\sin}^{\text{htf}}\\ \boldsymbol{G}_a^{\text{htf}}(s)\boldsymbol{A}_{\cos}^{\text{htf}} & V_{n,1}\boldsymbol{G}_a^{\text{htf}}(s)\boldsymbol{A}_{\sin}^{\text{htf}}\boldsymbol{G}_{\text{HPF}}^{\text{htf}}(s) & \boldsymbol{G}_a^{\text{htf}}(s)\left(\boldsymbol{I}-\boldsymbol{A}_{\sin}^{\text{htf}}\boldsymbol{G}_{\text{LPF}}^{\text{htf}}(s)\boldsymbol{A}_{\sin}^{\text{htf}}\right)\\ -\frac{1}{V_{n,-1}}\boldsymbol{G}_a^{\text{htf}}(s)\boldsymbol{A}_{\sin}^{\text{htf}} & \frac{V_{n,1}}{V_{n,-1}}\boldsymbol{G}_a^{\text{htf}}(s)\boldsymbol{A}_{\cos}^{\text{htf}}\boldsymbol{G}_{\text{HPF}}^{\text{htf}}(s)+h\boldsymbol{G}_b^{\text{htf}}(s) & \left(\frac{-1}{V_{n,1}}\boldsymbol{G}_b^{\text{htf}}(s)-\frac{1}{V_{n,-1}}\boldsymbol{G}_a^{\text{htf}}(s)\boldsymbol{A}_{\cos}^{\text{htf}}\boldsymbol{G}_{\text{LPF}}^{\text{htf}}(s)\right)\boldsymbol{A}_{\sin}^{\text{htf}}\end{bmatrix}$$
$$\begin{bmatrix}-V_{n,-1}\boldsymbol{G}_a^{\text{htf}}(s)\boldsymbol{A}_{\sin}^{\text{htf}}\\ \frac{V_{n,-1}}{V_{n,1}}\boldsymbol{G}_b^{\text{htf}}(s)\boldsymbol{A}_{\cos}^{\text{htf}}\\ -V_{n,-1}\boldsymbol{G}_a^{\text{htf}}(s)\boldsymbol{A}_{\sin}^{\text{htf}}\boldsymbol{G}_{\text{LPF}}^{\text{htf}}(s)\boldsymbol{A}_{\cos}^{\text{htf}}\\ \boldsymbol{G}_a^{\text{htf}}(s)\left(\boldsymbol{I}-\boldsymbol{A}_{\cos}^{\text{htf}}\boldsymbol{G}_{\text{LPF}}^{\text{htf}}(s)\boldsymbol{A}_{\cos}^{\text{htf}}\right)+\frac{hV_{n,-1}}{V_{n,1}}\boldsymbol{G}_b^{\text{htf}}(s)\boldsymbol{A}_{\cos}^{\text{htf}}\end{bmatrix}\begin{bmatrix}\boldsymbol{V}_{e,1}^{\text{htf}}(s)\\ \boldsymbol{\theta}_{e,1}^{\text{htf}}(s)\\ \boldsymbol{V}_{e,-1}^{\text{htf}}(s)\\ \boldsymbol{\theta}_{e,-1}^{\text{htf}}(s)\end{bmatrix}\tag{49}$$

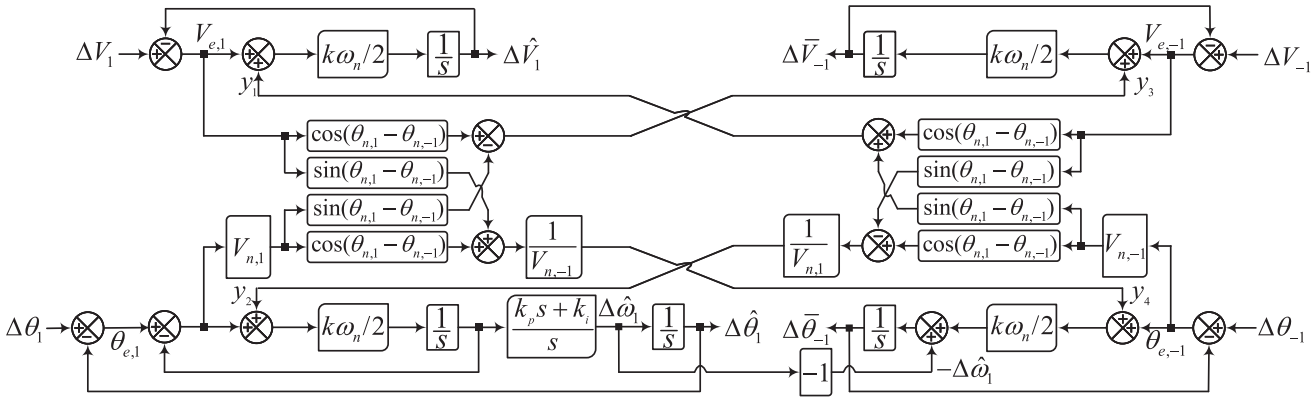

Fig. 33. LTP model of the DSOGI-PLL.

$$A_{\cos}^{\text{htf}}=\begin{bmatrix}\ddots & \ddots & \ddots & & \\ \ddots & 0 & \frac{e^{-j\varphi_{ps}}}{2} & 0 & \\ \ddots & \frac{e^{j\varphi_{ps}}}{2} & 0 & \frac{e^{-j\varphi_{ps}}}{2} & \ddots \\ & 0 & \frac{e^{j\varphi_{ps}}}{2} & 0 & \ddots \\ & & \ddots & \ddots & \ddots\end{bmatrix}$$

$$A_{\sin}^{\text{htf}}=\begin{bmatrix}\ddots & \ddots & \ddots & & \\ \ddots & 0 & \frac{je^{-j\varphi_{ps}}}{2} & 0 & \\ \ddots & -\frac{je^{j\varphi_{ps}}}{2} & 0 & \frac{je^{-j\varphi_{ps}}}{2} & \ddots \\ & 0 & -\frac{je^{j\varphi_{ps}}}{2} & 0 & \ddots \\ & & \ddots & \ddots & \ddots\end{bmatrix}. \tag{50}$$

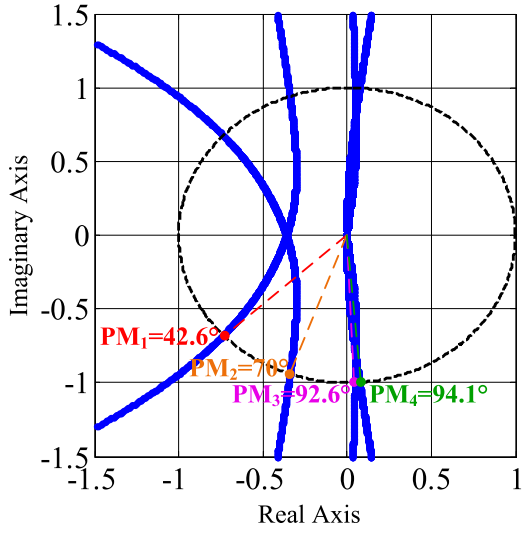

Fig. 34. Open-loop LTP Nyquist plot of the DSOGI-PLL. Control parameters are $k=\sqrt{2}$, $b=1+\sqrt{2}$, $k_p=\frac{k\omega_n}{2b}$, and $k_i=\frac{k^2\omega_n^2}{4b^3}$, which are the same as those in Figs. 33 and 30(a). Working point is $V_{n,1}=1$ p.u., $V_{n,-1}=0.5$ p.u., $\varphi_1=0$, and $\varphi_{-1}=\pi/6$ rad. The working point may considerably affects the LTP Nyquist plot.

Using the open-loop HTF (49), the open-loop LTP Nyquist plot of the DSOGI-PLL can be obtained, as shown in Fig. 34. Contrary to the LTI Nyquist plots in Figs. 10 and 30(a), the LTP one has four eigenvalue curves and, therefore, four eigenvalue PM and GM. The reason is that the LTP model of the DSOGI-PLL takes the effect of the fundamental negative sequence component of the grid voltage into account and, therefore, has four estimation loops (see Fig. 33). Note that PM_1 and PM_2 in Fig. 34 are roughly comparable to those in Fig. 30(a).

In Fig. 35, the variations of PM_1 of the DSOGI-PLL as a function of the SOGI gain k are observed. If we compare Fig. 35 with Fig. 31, the following observations can be made.

1) In both cases, PM_1 reduces with increasing the SOGI gain k and, therefore, the DSOGI-PLL's bandwidth. The rate of reduction, however, could be different based on the value of k.
2) The grid voltage imbalance adversely affects the stable range of the SOGI gain k. Note that this range is $k<3.88$ and $k<3.28$ according to Figs. 31 and 35, respectively. This negative effect becomes less significant by reducing the amplitude of the fundamental negative sequence component.

The abovementioned observations confirm that a high-bandwidth control design and the presence of disturbance components in the grid voltage both may lead to lower stability margins than those promised by the ESO tuning rule. In such cases, the design constant b could be set a bit higher to compensate for these negative effects.

VIII. Phase Lead Compensation

Sometimes, due to the large phase delay caused by a PF or IF, the application of the ESO tuning rule leads to a very low-bandwidth PLL with a slow dynamic response, which may not be desirable in some applications. For instance, consider the PLL designed for Scenario 3 in Table II, which uses an MAF with $T_w=0.02$ s. The 2% settling time of this PLL in response to the phase jump test [see Fig. 6(a)] is around 150 ms, which is quite long. A solution to deal with this problem is

TABLE IV
CONTROL PARAMETERS AND DETAILS OF THE RESULTS REPORTED IN FIGS. 37 AND 38. P2P: PEAK-TO-PEAK

	LC	Control parameters	Test 1 (see Fig. 37)		Test 2 (see Fig. 38)		PM
			2% settling time	Phase overshoot	P2P frequency error	P2P phase error	
MAF-PLL	No	$k_p = 41.4,\ k_i = 710.7$ $T_w = 0.02\ s$	148 ms	36%	0.01 Hz	0.17°	43.6°
	Yes	$k_p = 48.7,\ k_i = 983.6$ $T_w = 0.02\ s,\ \tau' = 0.01\ s$ $\alpha = 0.85$	127 ms	38%	0.015 Hz	0.25°	42.6°
	Yes	$k_p = 59.2,\ k_i = 1450.4$ $T_w = 0.02\ s,\ \tau' = 0.01\ s$ $\alpha = 0.7$	108 ms	42.9%	0.025 Hz	0.36°	40.8°

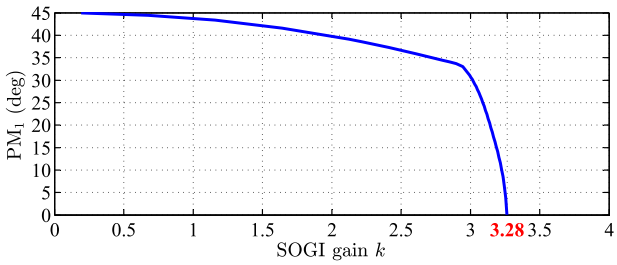

Fig. 35. Variations of an eigenvalue PM of the DSOGI-PLL as a function of the SOGI gain k. The open-loop HTF of the LTP model of the DSOGI-PLL is used for obtaining these results [see Fig. 34 and (49)]. Control parameters are $b = 1 + \sqrt{2}$, $k_p = \frac{k\omega_n}{2b}$, and $k_i = \frac{k^2\omega_n^2}{4b^3}$. Working point is $V_{n,1} = 1$ p.u., $V_{n,-1} = 0.5$ p.u., $\varphi_1 = 0$, and $\varphi_{-1} = \pi/6$ rad.

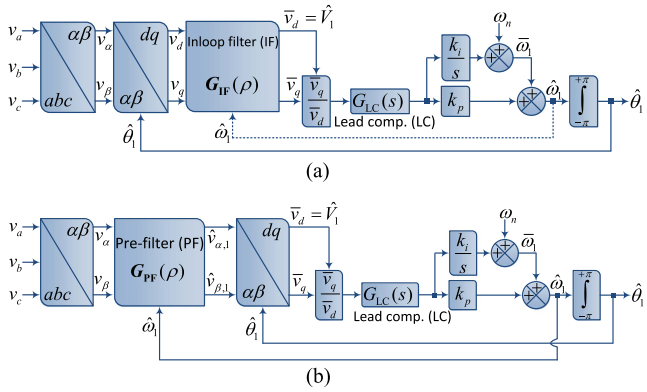

Fig. 36. Phase lead compensation in (a) a 3ϕ PLL equipped with an IF and (b) a 3ϕ PLL equipped with a PF. The dashed line indicates that the frequency feedback is not mandatory.

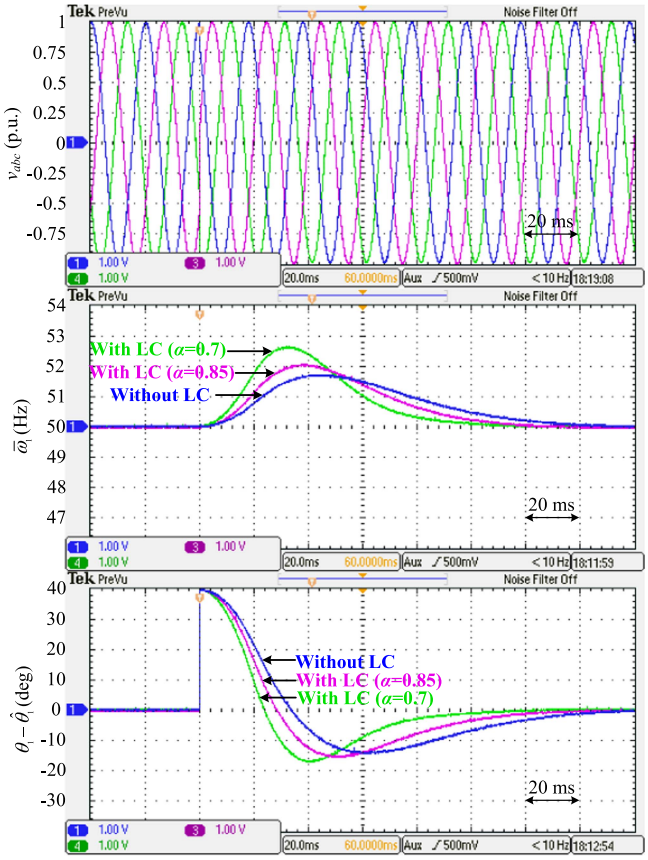

Fig. 37. Results of the PLL designed for Scenario 3 in Table II and its phase delay compensated versions under $+40°$ phase jump.

using a lead compensator (LC), as shown in Fig. 36. This idea, however, involves some modifications to the ESO-based tuning rule. To better understand this, consider Fig. 36(a), in which an LC is applied to compensate for the phase delay caused by the PLL's IF. In the presence of the LC, the tuning rule presented in Section II-B needs to be modified as follows.

1) Select an IF according to the expected disturbances in the grid voltage, and obtain its first-order approximation as $G_{\rm IF}(s) \approx \frac{1}{\tau s+1}$.
2) Consider the LC as $G_{\rm LC}(s) = \frac{\tau' s+1}{\alpha\tau' s+1}$, and arrange a pole-zero cancellation by selecting $\tau' = \tau$.
3) Select the factor α in the range of 0.7 to 1 depending on the required level of improvement in the speed of dynamic response.
4) Select the PI gains as $k_p = \frac{1}{b(\alpha\tau')}$ and $k_i = \frac{1}{b^3(\alpha\tau')^2}$.

A similar procedure as previous can be adopted for the case that the PLL is equipped with a PF.

In Figs. 37 and 38, the results of a comparison between the PLL designed for Scenario 3 in Table II and its phase delay compensated versions are observed. Based on these results, the following observations can be made.

1) Using the LC improves the speed of dynamic response (see Table IV for details). This improvement is proportional to the degree of phase lead caused by the LC.
2) The lead compensation results in a reduced PM (compared to the targeted value) and, therefore, an increased overshoot (see Table IV for details). The reason is that the phase lead compensation leads to a higher control bandwidth

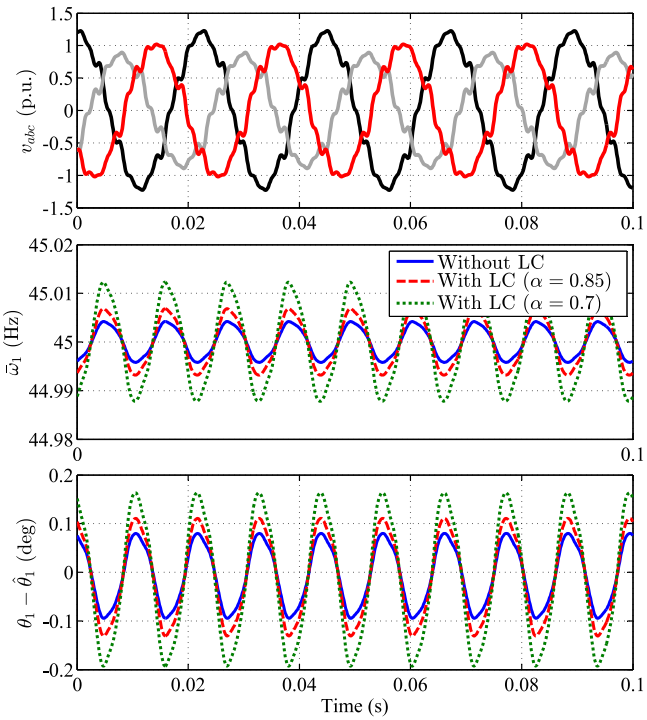

Fig. 38. Results of the PLL designed for Scenario 3 in Table II and its phase delay compensated versions under a harmonically distorted and imbalanced grid condition. The grid frequency is fixed at 45 Hz.

for the PLL and at higher frequencies, the accuracy of the first-order approximation of the IF (which is an MAF here) reduces. That is the reason why a limited phase lead compensation (i.e., $0.7 \leq \alpha < 1$) was recommended previously.

3) The lead compensation leads to a reduced noise immunity because, as mentioned previously, it results in a higher control bandwidth for the PLL.

IX. Discussion

A. Weak Grid Scenario

The common trend in designing grid synchronization systems is neglecting the dynamic interactions between them and grid-tied power converters. This assumption is valid for stiff ac systems, where the voltage at the point of common coupling is not affected (at least not considerably) by the converter output current. In weak grid scenarios, however, this assumption is not valid. Indeed, it has been proved that the grid synchronization system may have a noticeable impact on the stability of grid-tied power converters in weak grid conditions [8], [45], [46], [47], [48]. To prevent such stability issues, an interactive design concept may be adopted. This concept involves developing an initial design by neglecting the abovementioned interactions and refining it later using a trial-and-error procedure by taking these interactions into account. To this end, a complete numerical or analytical impedance model of the converter-grid system can be very helpful. The numerical model can be developed using a frequency scanning method, and the analytical one can be obtained by linearizing the GNDEs of the converter-grid system around the working point. These GNDEs take the dynamics of the grid synchronization system and converter's current controller into account. Detailed discussions about the analytical impedance modeling of grid-tied power converters equipped with advanced grid synchronization systems can be found in [8], [45], [46], [47], [48]. If needed, the dynamics of the dc-link voltage controller and machine-side converter (in case of wind systems) may also be included in the model. Using such a model, the impact of the grid synchronization unit on the stability of the entire converter-grid system can be investigated and the required refinements/modifications can be applied.

It is important to note that the parallel connection of converters can lead to a weak grid scenario or worsen an existing one. This fact has been proved in [49], which shows connecting converters with similar characteristics in parallel results in a multiplication of the equivalent grid inductance by the number of converters. To design the grid synchronization of converters in such a scenario, it is suggested to obtain an equivalent converter that models all converters in parallel and then follow the design method of this article, along with the discussions mentioned previously.

B. High-Bandwidth Control Design

Roughly speaking, 1ϕ PLLs often face stability issues in high-bandwidth implementations. The same goes for 3ϕ PLLs equipped with a notch-filter-like filter (e.g., an IIR NF, a cascaded *dq*DSC operator, and an MAF) in their structure. The reason is that the phase roll-off caused by such a filter makes the forward path phase to go below -180° around the notch frequency (for example, see Fig. 5), restricting a high-bandwidth implementation. Therefore, to achieve a high bandwidth, one should probably avoid such filters in the PLL structure or use a standard PLL without any IF/PF.

For PLLs with filters that restrict a high-bandwidth implementation, one may use a lead compensation and/or set the design constant b in the ESO tuning rule a bit higher. These measures may enable designers to achieve higher control bandwidths without jeopardizing stability. Interested readers are also referred to [50] and [51], which propose innovative methods for achieving a high-bandwidth implementation in some specific PLLs.

Note that the abovementioned discussions are also valid for FLLs because PLLs and FLLs have a close relationship [7].

C. Sampling Delay

In applications where the sampling frequency is low, the sampling delay is noticeable and, therefore, its impact needs to be considered in tuning the control parameters of the grid synchronization system. An example of such applications is the control of high-power converters, where the switching frequency and, therefore, the sampling frequency are often low to minimize the switching losses. To model the impact of the sampling delay, adding a simple lag term as $\frac{1}{T_s s+1}$ to the forward path of the PLL is suggested in [52], where T_s is the sampling time. It means that if, for example, (9) is the open-loop TF of a PLL without considering the sampling delay, then (51) is the open-loop with

this delay considered

$$G_{ol}^{\theta_1}(s) = \frac{1}{\tau s+1}\frac{1}{T_s s+1}\frac{k_p s+k_i}{s^2} \approx \frac{1}{(\tau+T_s)s+1}\frac{k_p s+k_i}{s^2}. \tag{51}$$

In this case, the result of applying the ESO tuning rule is

$$k_p = \frac{1}{b(\tau+T_s)}$$
$$k_i = \frac{1}{b^3(\tau+T_s)^2}. \tag{52}$$

X. Conclusion

The main objective of this article was to provide comprehensive guidelines to design the control parameters of different grid synchronization systems using the ESO tuning rule. The key idea was that after some rearrangements and linearizations, the low-frequency dynamics of many advanced PLLs and FLLs can be well-approximated by a standard type-2 control system and the ESO method can be applied to tune their control parameters. To better understand this idea, several case studies including PLLs and FLLs with different IFs/PFs were presented and their tuning using the ESO tuning rule was discussed. Some discussions about limitations of the ESO tuning rule and possible solutions to deal with them were also presented.

The design procedure proposed in this article, along with the accompanying discussions, have been summarized in a clear and easy-to-follow flowchart depicted in Fig. 39. This design procedure make the control tuning of grid synchronization systems more efficient and straightforward, even for those with limited experience in control and signal processing areas.

Appendix A
First-Order Approximation of (16)

By replacing $s = j\omega$, the phase characteristic of (16) can be expressed as

$$\angle\bar{G}_r(j\omega) = \tan^{-1}\left(\frac{4\omega_n^2\omega-\omega^3}{2k\omega_n^3-k\omega_n\omega^2}\right) - \tan^{-1}\left(\frac{4k\omega_n^3\omega-2k\omega_n\omega^3}{\omega^4-(k^2+4)\omega_n^2\omega^2+k^2\omega_n^4}\right). \tag{A-1}$$

In the low-frequency range, the second and higher terms of ω have a small effect. If we neglect these terms, we get

$$\angle\bar{G}_r(j\omega) \approx \tan^{-1}\left(\frac{4\omega_n^2\omega}{2k\omega_n^3}\right) - \tan^{-1}\left(\frac{4k\omega_n^3\omega}{k^2\omega_n^4}\right)$$
$$= \tan^{-1}\left(\frac{2}{k\omega_n}\omega\right) - \tan^{-1}\left(\frac{4}{k\omega_n}\omega\right)$$
$$\approx -\tan^{-1}\left(\frac{2}{k\omega_n}\omega\right). \tag{A-2}$$

A first-order lag filter with the time-constant $\tau = 2/(k\omega_n)$ has the same phase characteristic as previous. Therefore, (16) can

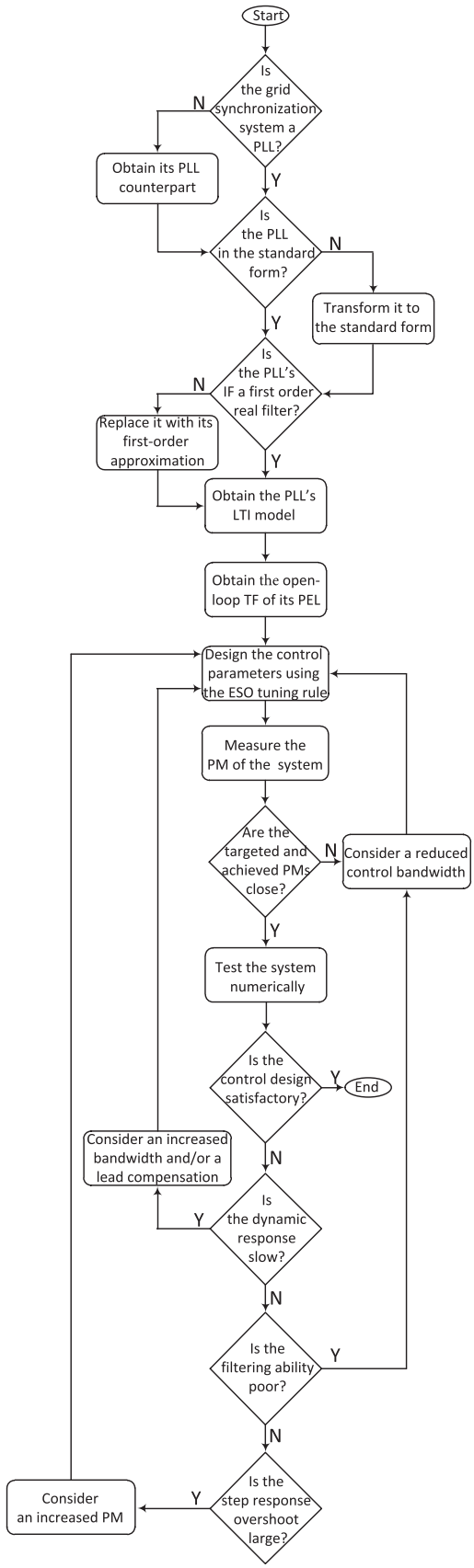

Fig. 39. Flowchart of the proposed design procedure. A standard-form PLL refers to a PLL as in Fig. 7(c).

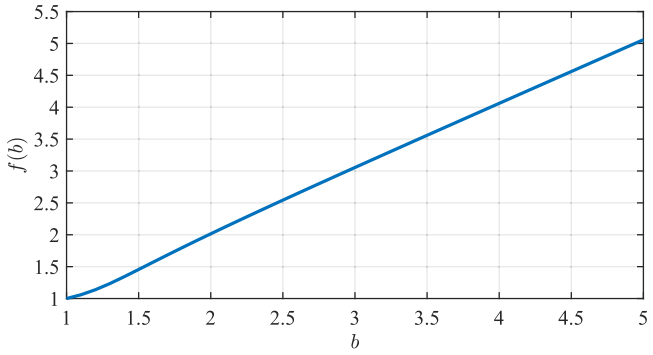

Fig. 40. Variations of $f(b)$ as a function of the design constant b. $f(b) = \omega_c'/\omega_c$, where ω_c' and ω_c are the gain crossover frequencies of the phase and FELs of the ST3-PLL in Fig. 17(a).

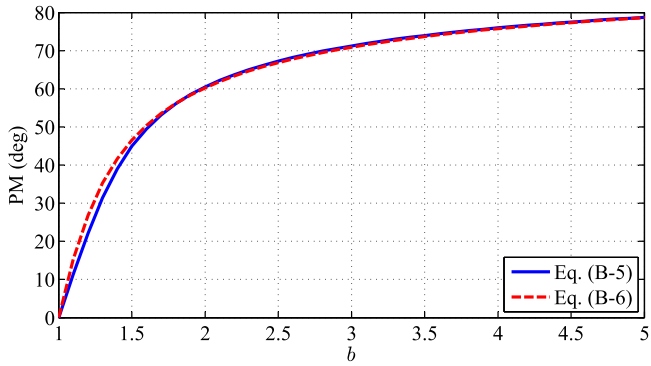

Fig. 41. Variations of the PM of the PEL as a function of the design constant b.

be well-approximated in the low-frequency range with

$$\bar{G}_r(s) \approx \frac{1}{\underbrace{(2/(k\omega_n))}_{\tau}\, s + 1}. \tag{A-3}$$

Appendix B
PM of the PEL of the ST3-PLL

If we replace k_p, k_i, and k_a in the open-loop TF (32) with their corresponding expressions in (34), it can be rewritten as

$$G_{ol}^{\theta_1}(s) = \frac{b\omega_c s^2 + b\omega_c^2 s + \omega_c^3}{s^3}. \tag{B-1}$$

If we replace $s = j\omega$ in (B-1), we get

$$G_{ol}^{\theta_1}(j\omega) = \frac{-b\omega_c\omega^2 + jb\omega_c^2\omega + \omega_c^3}{-j\omega^3} = \frac{-b(\omega/\omega_c)^2 + jb\omega/\omega_c + 1}{-j(\omega/\omega_c)^3}. \tag{B-2}$$

Given that ω_c' is the gain crossover frequency of the abovementioned open-loop TF, we have

$$\left|G_{ol}^{\theta_1}(j\omega_c')\right| = \frac{\sqrt{\left[1 - b(\omega_c'/\omega_c)^2\right]^2 + \left[b\omega_c'/\omega_c\right]^2}}{(\omega_c'/\omega_c)^3} = 1. \tag{B-3}$$

If we define $x = \omega_c'/\omega_c$ and square both sides of the abovementioned equation, we get

$$x^6 - b^2x^4 - (b^2 - 2b)x^2 - 1 = 0. \tag{B-4}$$

The positive solution of the abovementioned equation is the desired solution. This solution may be expressed as $x = \omega_c'/\omega_c = f(b) > 0$ where $f(b)$ is a function of the design constant b. Fig. 40 shows the variations of $f(b)$ as a function of b. This plot indicates that $f(b) \approx b$.

Using (B-1), the PM of the PEL is determines as

$$\mathrm{PM} = 180^\circ + \angle G_{ol}^{\theta_1}(j\omega_c') = 90^\circ + \tan^{-1}\left(\frac{b\omega_c'/\omega_c}{1 - b(\omega_c'/\omega_c)^2}\right) = 90^\circ + \tan^{-1}\left(\frac{bf(b)}{1 - bf^2(b)}\right). \tag{B-5}$$

It is observed that the PM is only a function of the design constant b. If we replace $f(b) \approx b$ in the abovementioned equation, we get

$$\mathrm{PM} \approx 90^\circ + \tan^{-1}\left(\frac{b^2}{1 - b^3}\right) = \tan^{-1}\left(\frac{b^3 - 1}{b^2}\right). \tag{B-6}$$

The abovementioned equation is an accurate approximation of (B-5). Fig. 41, which provides a numerical comparison between (B-5) and (B-6), confirms this accuracy.

References

[1] S. Golestan, J. M. Guerrero, and J. C. Vasquez, "Three-phase PLLs: A review of recent advances," *IEEE Trans. Power Electron.*, vol. 32, no. 3, pp. 1894–1907, Mar. 2017.

[2] S. Golestan, J. M. Guerrero, and J. C. Vasquez, "Single-phase PLLs: A review of recent advances," *IEEE Trans. Power Electron.*, vol. 32, no. 12, pp. 9013–9030, Dec. 2017.

[3] S. Golestan, J. M. Guerrero, J. C. Vasquez, A. M. Abusorrah, and Y. Al-Turki, "A study on three-phase FLLs," *IEEE Trans. Power Electron.*, vol. 34, no. 1, pp. 213–224, Jan. 2019.

[4] S. Golestan, J. M. Guerrero, F. Musavi, and J. C. Vasquez, "Single-phase frequency-locked loops: A comprehensive review," *IEEE Trans. Power Electron.*, vol. 34, no. 12, pp. 11791–11812, Dec. 2019.

[5] S. C. Gulipalli, S. Gude, S.-C. Peng, and C.-C. Chu, "Multiple delayed signal cancellation filter-based enhanced frequency-locked loop under adverse grid conditions," *IEEE Trans. Ind. Appl.*, vol. 58, no. 5, pp. 6612–6628, Sep./Oct. 2022.

[6] H. Zheng, Z. Liu, R. An, J. Liu, K. Feng, and Y. Tu, "Discrete multiple second-order generalized integrator with low-pass filters and frequency-locked loop for DC rejection," *IEEE Trans. Power Electron.*, vol. 37, no. 10, pp. 11814–11827, Oct. 2022.

[7] S. Golestan, J. M. Guerrero, M. J. Rawa, A. M. Abusorrah, and Y. Al-Turki, "Frequency-locked loops in electrical power and energy systems: Equivalent or different to phase-locked loops?," *IEEE Ind. Electron. Mag.*, vol. 15, no. 4, pp. 54–64, Dec. 2021.

[8] S. Golestan, J. M. Guerrero, Y. Al-Turki, J. C. Vasquez, and A. M. Abusorrah, "Impedance modeling of three-phase grid-connected voltage source converters with frequency-locked-loop-based synchronization algorithms," *IEEE Trans. Power Electron.*, vol. 37, no. 4, pp. 4511–4525, Apr. 2022.

[9] E. Guest and N. Mijatovic, "Discrete-time complex bandpass filters for three-phase converter systems," *IEEE Trans. Ind. Electron.*, vol. 66, no. 6, pp. 4650–4660, Jun. 2019.

[10] W. Shi, J. Yu, J. Yu, and R. Zhou, "A low computational cost ROGI-based frequency-locked loop," *IEEE J. Emerg. Sel. Topics Ind. Electron.*, vol. 3, no. 3, pp. 860–865, Jul. 2022.

[11] S. Golestan, M. Ramezani, J. M. Guerrero, F. D. Freijedo, and M. Monfared, "Moving average filter based phase-locked loops: Performance analysis and design guidelines," *IEEE Trans. Power Electron.*, vol. 29, no. 6, pp. 2750–2763, Jun. 2014.

[12] H. Khazraj, F. F. d. Silva, C. L. Bak, and S. Golestan, "Analysis and design of notch filter-based PLLs for grid-connected applications," *Electric Power Syst. Res.*, vol. 147, pp. 62–69, 2017.

[13] C. Kessler, "Das symmetrische optimum, teil I," *At-Automatisierungstechnik*, vol. 6, no. 1–12, pp. 395–400, 1958.

[14] C. Kessler, "Das symmetrische optimum, teil II," *At-Automatisierungstechnik*, vol. 6, no. 1–12, pp. 432–436, 1958.

[15] K. J. Åström and T. Hägglund, *PID Controllers: Theory, Design, and Tuning*. Pittsburgh, PA, USA: International Society of Automation, 1995.

[16] S. Preitl and R.-E. Precup, "An extension of tuning relations after symmetrical optimum method for PI and PID controllers," *Automatica*, vol. 35, no. 10, pp. 1731–1736, 1999.

[17] X. Li and F. Gao, "A three-sample filter for fast arbitrary harmonic elimination," *IEEE Trans. Ind. Electron.*, vol. 69, no. 5, pp. 5122–5131, May 2022.

[18] S. Gude, C.-C. Chu, and S. V. Vedula, "Recursive implementation of multiple delayed signal cancellation operators and their applications in prefiltered and in-loop filtered PLLs under adverse grid conditions," *IEEE Trans. Ind. Appl.*, vol. 55, no. 5, pp. 5383–5394, Sep./Oct. 2019.

[19] S. Golestan, F. D. Freijedo, and J. M. Guerrero, "A systematic approach to design high-order phase-locked loops," *IEEE Trans. Power Electron.*, vol. 30, no. 6, pp. 2885–2890, Jun. 2015.

[20] F. D. Freijedo, A. G. Yepes, O. Lopez, P. Fernandez-Comesana, and J. Doval-Gandoy, "An optimized implementation of phase locked loops for grid applications," *IEEE Trans. Instrum. Meas.*, vol. 60, no. 9, pp. 3110–3119, Sep. 2011.

[21] Y. F. Wang and Y. W. Li, "Analysis and digital implementation of cascaded delayed-signal-cancellation PLL," *IEEE Trans. Power Electron.*, vol. 26, no. 4, pp. 1067–1080, Apr. 2011.

[22] C. Liu, J. Jiang, J. Jiang, and Z. Zhou, "Enhanced grid-connected phase-locked loop based on a moving average filter," *IEEE Access*, vol. 8, pp. 5308–5315, 2020.

[23] S. Golestan, M. Monfared, F. D. Freijedo, and J. M. Guerrero, "Performance improvement of a prefiltered synchronous-reference-frame PLL by using a PID-type loop filter," *IEEE Trans. Ind. Appl. Electron.*, vol. 61, no. 7, pp. 3469–3479, Jul. 2014.

[24] J. I. Garcia, J. I. Candela, and P. Catalán, "Prefiltered synchronization structure for grid-connected power converters to reduce the stability impact of PLL dynamics," *IEEE J. Emerg. Sel. Topics Power Electron.*, vol. 9, no. 5, pp. 5499–5507, Oct. 2021.

[25] K. Liu, W. Cao, J. Zhao, and J. You, "Unified digital phase-locked loop with multiple complex resonators for both single- and three-phase grid synchronization," *IEEE Access*, vol. 5, pp. 24810–24818, 2017.

[26] S. Golestan, A. Akhavan, J. M. Guerrero, A. M. Abusorrah, M. J. H. Rawa, and J. C. Vasquez, "In-loop filters and prefilters in phase-locked loop systems: Equivalent or different solutions?," *IEEE Ind. Electron. Mag.*, vol. 16, no. 3, pp. 23–35, Sep. 2022.

[27] P. Rodríguez, R. Teodorescu, I. Candela, A. V. Timbus, M. Liserre, and F. Blaabjerg, "New positive-sequence voltage detector for grid synchronization of power converters under faulty grid conditions," in *Proc. 37th IEEE Power Electron. Specialists Conf.*, 2006, pp. 1–7.

[28] P. Rodriguez, A. Luna, R. S. Munoz-Aguilar, I. Etxeberria-Otadui, R. Teodorescu, and F. Blaabjerg, "A stationary reference frame grid synchronization system for three-phase grid-connected power converters under adverse grid conditions," *IEEE Trans. Power Electron.*, vol. 27, no. 1, pp. 99–112, Jan. 2012.

[29] S. Golestan, M. Monfared, F. D. Freijedo, and J. M. Guerrero, "Design and tuning of a modified power-based PLL for single-phase grid-connected power conditioning systems," *IEEE Trans. Power Electron.*, vol. 27, no. 8, pp. 3639–3650, Aug. 2012.

[30] I. Carugati, P. Donato, S. Maestri, D. Carrica, and M. Benedetti, "Frequency adaptive PLL for polluted single-phase grids," *IEEE Trans. Power Electron.*, vol. 27, no. 5, pp. 2396–2404, May 2012.

[31] R. M. Santos Filho, P. F. Seixas, P. C. Cortizo, L. A. B. Torres, and A. F. Souza, "Comparison of three single-phase PLL algorithms for UPS applications," *IEEE Trans. Ind. Electron.*, vol. 55, no. 8, pp. 2923–2932, Aug. 2008.

[32] C. Zhang, S. Føyen, J. A. Suul, and M. Molinas, "Modeling and analysis of SOGI-PLL/FLL-based synchronization units: Stability impacts of different frequency-feedback paths," *IEEE Trans. Energy Convers.*, vol. 36, no. 3, pp. 2047–2058, Sep. 2021.

[33] J. Xu, H. Qian, S. Bian, Y. Hu, and S. Xie, "Comparative study of single-phase phase-locked loops for grid-connected inverters under non-ideal grid conditions," *CSEE J. Power Energy Syst.*, vol. 8, no. 1, pp. 155–164, 2022.

[34] Y. Zhou, H. Hu, X. Yang, Z. Meng, and Z. He, "Impacts of quadrature signal generation-based PLLs on low-frequency oscillation in an electric railway system," *IEEE Trans. Transp. Electrific.*, vol. 7, no. 4, pp. 3124–3136, Dec. 2021.

[35] C. K. Aravind, B. I. Rani, C. Manickam, J. M. Guerrero, S. I. Ganesan, and C. Nagamani, "Performance evaluation of type-3 PLLs under wide variation in input voltage and frequency," *IEEE Trans. Emerg. Sel. Topics Power Electron.*, vol. 5, no. 3, pp. 971–981, Sep. 2017.

[36] S. Golestan, J. M. Guerrero, A. M. Abusorrah, J. C. Vasquez, and Y. Al-Turki, "LTP modeling and stability assessment of multiple second-order generalized integrator-based signal processing/synchronization algorithms and their close variants," *IEEE Trans. Power Electron.*, vol. 37, no. 5, pp. 5062–5077, May 2022.

[37] S. Golestan, M. Monfared, F. D. Freijedo, and J. M. Guerrero, "Advantages and challenges of a type-3 PLL," *IEEE Trans. Power Electron.*, vol. 28, no. 11, pp. 4985–4997, Nov. 2013.

[38] A. Bamigbade, V. Khadkikar, and M. A. Hosani, "A type-3 PLL for single-phase applications," *IEEE Trans. Ind. Appl.*, vol. 56, no. 5, pp. 5533–5542, Sep./Oct. 2020.

[39] P. Kanjiya, V. Khadkikar, and M. S. E. Moursi, "Obtaining performance of type-3 phase-locked loop without compromising the benefits of type-2 control system," *IEEE Trans. Power Electron.*, vol. 33, no. 2, pp. 1788–1796, Feb. 2018.

[40] Y. Wang et al., "A forward compensation method to eliminate DC phase error in SRF-PLL," *IEEE Trans. Power Electron.*, vol. 37, no. 6, pp. 6280–6284, Jun. 2022.

[41] S. Bifaretti, P. Zanchetta, and E. Lavopa, "Comparison of two three-phase PLL systems for more electric aircraft converters," *IEEE Trans. Power Electron.*, vol. 29, no. 12, pp. 6810–6820, Dec. 2014.

[42] H. A. Hamed and M. S. El Moursi, "A new type-2 PLL based on unit delay phase angle error compensation during the frequency ramp," *IEEE Trans. Power Syst.*, vol. 34, no. 4, pp. 3289–3293, Jul. 2019.

[43] S. Golestan, F. D. Freijedo, A. Vidal, J. M. Guerrero, and J. Doval-Gandoy, "A quasi-type-1 phase-locked loop structure," *IEEE Trans. Power Electron.*, vol. 29, no. 12, pp. 6264–6270, Dec. 2014.

[44] S. Golestan, J. M. Guerrero, J. C. Vasquez, A. M. Abusorrah, and Y. Al-Turki, "Harmonic linearization and investigation of three-phase parallel-structured signal decomposition algorithms in grid-connected applications," *IEEE Trans. Power Electron.*, vol. 36, no. 4, pp. 4198–4213, Apr. 2021.

[45] L. Harnefors, M. Bongiorno, and S. Lundberg, "Input-admittance calculation and shaping for controlled voltage-source converters," *IEEE Trans. Ind Electron.*, vol. 54, no. 6, pp. 3323–3334, Dec. 2007.

[46] M. Cespedes and J. Sun, "Impedance modeling and analysis of grid-connected voltage-source converters," *IEEE Trans. Power Electron.*, vol. 29, no. 3, pp. 1254–1261, Mar. 2014.

[47] B. Wen, D. Boroyevich, R. Burgos, P. Mattavelli, and Z. Shen, "Analysis of D-Q small-signal impedance of grid-tied inverters," *IEEE Trans. Power Electron.*, vol. 31, no. 1, pp. 675–687, Jan. 2016.

[48] S. Golestan, E. Ebrahimzadeh, B. Wen, J. M. Guerrero, and J. C. Vasquez, "dq-frame impedance modeling of three-phase grid-tied voltage source converters equipped with advanced PLLs," *IEEE Trans. Power Electron.*, vol. 36, no. 3, pp. 3524–3539, Mar. 2021.

[49] J. L. Agorreta, M. Borrega, J. López, and L. Marroyo, "Modeling and control of N -paralleled grid-connected inverters with LCL filter coupled due to grid impedance in PV plants," *IEEE Trans. Power Electron.*, vol. 26, no. 3, pp. 770–785, Mar. 2011.

[50] F. D. Freijedo, A. G. Yepes, O. Lopez, A. Vidal, and J. Doval-Gandoy, "Three-phase PLLs with fast postfault retracking and steady-state rejection of voltage unbalance and harmonics by means of lead compensation," *IEEE Trans. Power Electron.*, vol. 26, no. 1, pp. 85–97, Jan. 2011.

[51] S. Golestan, J. Matas, A. M. Abusorrah, and J. M. Guerrero, "More-stable EPLL," *IEEE Trans. Power Electron.*, vol. 37, no. 1, pp. 1003–1011, Jan. 2022.

[52] V. Kaura and V. Blasko, "Operation of a phase locked loop system under distorted utility conditions," *IEEE Trans. Ind. Appl.*, vol. 33, no. 1, pp. 58–63, Jan./Feb. 1997.